THERMAL FINITE ELEMENT MODEL TO COMPUTE MELT POOL DIMENSIONS FOR DIRECTED ENERGY DEPOSITION ADDITIVE MANUFACTURING PROCESS WITH EXPERIMENTAL VALIDATION

by

KEREM DÖRTKAŞLI

Submitted to the Graduate School of Engineering and Natural Sciences

in partial fulfillment of

the requirements for the degree of

Master of Science

SABANCI UNIVERSITY

JUNE 2021

THERMAL FINITE ELEMENT MODEL TO COMPUTE MELT POOL DIMENSIONS FOR DIRECTED ENERGY DEPOSITION ADDITIVE MANUFACTURING PROCESS WITH EXPERIMENTAL VALIDATION

APPROVED BY:

DATE OF APPROVAL:

ABSTRACT

THERMAL FINITE ELEMENT MODEL TO COMPUTE MELT POOL DIMENSIONS FOR DIRECTED ENERGY DEPOSITION ADDITIVE MANUFACTURING PROCESS WITH EXPERIMENTAL VALIDATION

KEREM DÖRTKAŞLI

Manufacturing Engineering, M.Sc. Thesis, June 2021

Thesis Supervisor: Assist. Prof. Dr. Eralp Demir

Keywords: Additive Manufacturing, Directed Energy Deposition, 3D Printing, Thermal Process Model, FEM

Directed energy deposition (DED), a metal additive manufacturing process, is the manufacturing of parts in layers by injecting metal powder into the melt pool created by the thermal energy provided by a heat source. Compared to traditional subtractive manufacturing methods, DED attracts attention as an emerging manufacturing technology in different industries with the reduction in using molds and tools, the need for assembly, the ability to design and manufacture parts with complex features, and the ability to manufacture on parts that need repair. Because of the nature of the process, the high temperature and temperature gradients that occur with high heat input are critical and still very important factors for directed energy deposition, just as with other additive manufacturing methods. The correct estimation of the structure and geometry of the melt pool and the effect it creates for the manufactured part during the process significantly affect the quality of the part.

For this purpose, in this thesis, a thermal finite element process model has been developed to better understand and predict the melt pool geometry and properties. The model includes temperature and state-dependent physical properties for materials used in the additive manufacturing process with novel features, treatment of surface losses as a volumetric heat flux to eliminate the need for the re-definition of the surface after the addition of each layer with an additional user-defined subroutine and evaporative heat losses added to the surface losses to avoid the high temperatures. To observe the effect of laser power and scanning speed on the structure of the melt pool, single-track and multi-layer samples were additively manufactured with Inconel 718 material for comparison and validation with the developed model. In experimental methods, the in-situ collected data using an infrared thermal camera were prepared and analyzed via developed image process method and used in comparison

with the model for melt pool area prediction. In addition, ex-situ melt pool characterization with an optical microscope was also examined, and the obtained findings were used for comparison with the developed model. The proposed thermal model accurately estimates the melt pool sizes in terms of area, depth, and width of both single-track and multi-layer depositions and inter-layer boundaries for multi-layer depositions with revealing the effect of laser power and scanning speed process parameters.

ÖZET

DENEYSEL DOĞRULAMA İLE YÖNLENDİRİLMİŞ ENERJİ BİRİKTİRME EKLEMELİ İMALAT SÜRECİ İÇİN ERGİYİK HAVUZU BOYUTLARINI HESAPLAMA İLE TERMAL SONLU ELEMAN MODELİ

KEREM DÖRTKAŞLI

Üretim Mühendisliği Yüksek Lisans Tezi, Haziran 2021

Tez Danışmanı: Dr. Öğretim Üyesi Eralp Demir

Anahtar Kelimeler: Eklemeli İmalat, Yönlendirilmiş Enerji Biriktirme, 3B Yazıcı, Termal Süreç Modeli, Sonlu Elemanlar Metodu

Bir eklemeli imalat süreci olan yönlendirilmiş enerji biriktirme, bir ısı kaynağı tarafından sağlanan termal enerjinin oluşturduğu ergiyik havuzuna metal tozu enjekte edilerek parçaların katmanlar halinde üretilmesidir. Geleneksel eksiltmeli üretim yöntemleriyle karşılaştırıldığında, yönlendirilmiş enerji biriktirme, kalıp ve alet kullanımının azalması, montaj ihtiyacının azalması, karmaşık özelliklere sahip parçaların tasarlanıp üretilebilmesi ve onarım gerektiren parçalar üzerinde üretim yapabilme yeteneği ile farklı endüstrilerde ortaya çıkan bir üretim teknolojisi olarak dikkat çekmektektedir. Sürecin doğası gereği, yüksek ısı girdisi ile ortaya çıkan yüksek sıcaklık ve sıcaklık gradyanları, diğer eklemeli imalat yöntemlerinde olduğu gibi, yönlendirilmiş enerji biriktirme için de kritik ve hala çok önemli faktörlerdir. Eriyik havuzunun yapısının ve geometrisinin doğru tahmin edilmesi ve süreç boyunca üretilen parça için yarattığı etki, parçanın nihai kalitesini büyük ölçüde etkiler.

Bu çalışmada, ergiyik havuzu özelliklerini bir süreç simülasyon modeli ile daha iyi anlamak ve tahmin etmek için bir termal sonlu eleman analizi geliştirilmiştir. Model içerisinde kullanılan metal malzemeler için, sıcaklık ve hale bağımlı olan fiziksel özellikler kullanılmıştır. Modelde özgün olarak yüzey kayıplarının hacimsel bir ısı akışı olarak işlenmesi uygunlanmış, ve her bir katmanın ilave bir kullanıcı tanımlı altprogram ile eklenmesinden sonra yüzeyin yeniden tanımlanması ihtiyacı ortadan kaldırılmıştır. Ayrıca, yüksek sıcaklıklardan kaçınmak için yüzey kayıplarına eklenen buharlaştırıcı ısı kayıpları modele dahil edilmiştir. Süreç için kritik önem taşıyan süreç parametlerinden olan lazer gücünün ve tarama hızının ergiyik havuzunun yapısı üzerindeki etkisini gözlemlemek için, geliştirilen model ile karşılaştırma ve doğrulama amacıyla Inconel 718 metal malzeme ile tek ve çok katmanlı numuneler imal edilmiştir. Deneysel yöntemlerde, tezgah içerisine

yerleştirilen kızıl ötesi termal kamera kullanılarak süreç içi yerinde toplanan veriler, geliştirilmiş olan görüntü işleme yöntemi ile hazırlanıp analiz edilmiş ve ergiyik havuzu alanı tahmini için model ile karşılaştırmak üzere kullanılmıştır. Ayrıca, imalat sonrası optik mikroskop ile numunelerin kesit alanları üzerinden ergiyik havuzu karakterizasyonu da incelenmiş ve elde edilen bulgular geliştirilen termal model ile karşılaştırılmıştır. Önerilen termal model, ergiyik havuzu boyutlarını hem tek katmanlı hem de çok katmanlı numuneler için ergiyik havuzu alanı, derinliği ve genişliği açısından ve lazer gücünün ile tarama hızı süreç parametrelerinin etkisiyle çok katmanlı numuneler için katmanlar arası sınırlar açısından düşük hata değerleri ile hassas bir şekilde tahmin etmektedir.

ACKNOWLEDGEMENTS

I want to extend my most special and sincere thanks to my thesis supervisor Asst. Prof. Dr. Eralp Demir for his guidance, supportive and constructive attitude throughout my master's degree. I will always be grateful to him for his never-ending support throughout our research studies, for his confidence in me always, and most of all for his encouragement on me to write this thesis. I want to thank him for tirelessly answering every question I ask, and never ceasing to enlighten me on matters I do not have knowledge. I am very proud to be one of his students.

I would also like to thank Dr. Murat Işık and M.Sc. Ragıp Orkun Seçer for informing me deeply about emerging additive manufacturing technologies and spending much time supporting me to carry out the manufacturing and experiments smoothly.

My profound thanks go to my colleagues, friends and administrative staff of Sabanci University and Sabanci University Integrated Manufacturing Research and Application Center. I feel exceptional and lucky since they helped me no matter what time it is, every time I requested during my study. I would like to thank all my close friends for their support and encouragement during this stage of my life and for being by my side when I need to clear my head and have fun.

Finally, I would like to thank my family for the love and affection they have shown since my childhood, encouragement, and endless patience throughout my thesis stage and entire life journey. I would like to express my most special thanks to my nephew for being my joy who was born during my thesis stage. Since the day he joined our family, I have felt more fortunate, blessed, and happy, and I thought that his luck is on my side if I completed this thesis. I hope and believe that when he grows up, one day he will also research an area that he is passionate about and want to improve himself and will be very successful.

TABLE OF CONTENTS

LIST OF FIGURES

LIST OF TABLES

LIST OF ABBREVIATIONS

2D: Two-Dimensional

3D: Three-Dimensional

3DP: Three-Dimensional Printing

AED: Areal Energy Density

AM: Additive Manufacturing

ASTM: American Society for Testing and Materials

CAD: Computer Aided Design

DED: Directed Energy Deposition

DfAM: Design for Additive Manufacturing

DMD: Directed Metal Deposition

DMLM: Direct Metal Laser Melting

EBM: Electron Beam Melting

EDM: Electrical Discharge Machining

FDM: Fused Deposition Modeling

FEM: Finite Element Method

HAZ: Heat Affected Zone

IN718: Inconel 718

IR: Infra-red

K: Kelvin

LC: Laser Cladding

LDS: Laser Displacement Sensor

LED: Linear Energy Density

LENS™: Laser Engineered Net Shaping

LM: Layer Manufacturing

LMD: Laser Metal Deposition

LOM: Laminated Object Fabrication

OM: Optical Microscopy

PBF: Powder Bed Fusion

RP: Rapid Prototyping

SGC: Solid Ground Curing

SLS: Selective Laser Sintering

SLM: Selective Laser Melting

SS316L: Stainless Steel Grade 316L

UV: Ultraviolet

VED: Volumetric Energy Density

WAAM: Wire Arc Additive Manufacturin

1. INTRODUCTION

1.1 Overview

Implementing additive manufacturing (AM) process to production capabilities has been increasing with a rising trend in the manufacturing industry, especially since the early 2000s, and it continues to gain more importance every year. According to the definition of the American Society for Testing and Materials (ASTM), AM is described as "Combining materials to make objects from 3D model data, usually layer on layer, as opposed to traditional subtractive manufacturing methodologies [1]."

Along with the critical advancements in the emerging technologies and processes, researchers on the subject in recent years have focused on improving additive manufacturing machines and the restrictions that may cause difficulties in manufacturing the part. In the processes used by metal materials, which is the most used additive manufacturing method in producing value-added parts, researchers have focused on a few issues on obtaining parts defined as near net shape for the end-user that are meeting the functional criteria. Besides the slicing algorithms achieved by computer-aided software, which are called pre-process before the part production, there are studies to improve the user's parameters during the process.

However, it turns out that the investigations by focusing on the geometric constraints allowed by the part and the machine do not improve the process sufficiently. With this information, additive manufacturing technology, and especially the physics of metal additive manufacturing technology because of the complex physics because of nature of the process, should be studied and examined in more detail.

Nonetheless, the metal additive manufacturing modeling studies are carried out, and these research reveal detailed examinations can be carried out regarding thermal modeling of metal additive manufacturing. By creating a thermal model that has been revealed by examining the process, the temperature distribution on the part, the thermal history, the effect of heat input on the part, and the structure of the melt pool geometry and dimensions, which is the most complex point of this input, can be examined. The effect gives to the part during the manufacturing process and converges to actual cases. Besides, thanks to such a thermal

additive manufacturing model, it will be possible to capture and examine the effects of the critical parameters of the additive manufacturing process on the thermal structure on the part with the values specified as input by simulating the manufacturing process on the model. By eliminating the trial-and-error process, it will save users both time and cost.

1.2 Aim and Outline

In the studies on the additive manufacturing process modeling, the melt pool's physics-based properties are not always considered in thermal model solutions, and the thermal and mechanical problems that the melt pool geometry will create on the part cannot be captured. As an example of these analytical models developed insufficient of integrating the process into 3-dimensional (3D) structures. Models based on the finite element method (FEM) offer more valuable solutions in this sense and come with a very high computation time required to model the entire process. They cannot have the solution speed of a thermal model that focuses explicitly on the geometry of the melt pool.

The research carried out includes the investigation of directed energy deposition (DED) method, one type of the metal AM processes. The heat source (laser or electron beam) selected in this method melts the powder deposited coaxially according to the previously created 3D design and repeats for each layer determined until the fabrication is completed by feeding the melt pool created in the previous layer with metal powder. However, this process brings difficulties because the process and modeling gain importance in this sense. As the laser moves away from the melted area, depending on the material properties, geometry, and process parameters, the cooling phase starts, and the material becomes solid after a while. For this reason, the thermal model to be developed must observe both the phase formed because of the interaction with the laser and powder during the post-solidification state.

Therefore, the aim of this thesis is to create a FEM thermal model. It comprises the material properties and process parameters used for the directed energy deposition method, their effects on the temperature distribution and melt pool geometry during manufacturing. The thermal model, which includes the material phase transformations and a user-defined 3D heat source model, together with the heat input to which the material is exposed, predicted the temperature change and the geometry of the molten pool generates in the deposited layer.

In this thesis study, a thermal FEM is developed inside a commercial finite element software by user subroutines for more accurate simulations of DED process by element activation methods considering temperature and state dependent material properties. The novel features of the model are:

- Treatment of surface losses as a volumetric heat flux to eliminate the need for the re-definition of surface after the addition of each layer with an additional user defined subroutine.
- Evaporative heat losses added to the surface losses to avoid the high temperatures.

The model results are compared with in-situ experimental measurements of the temperatures and melt pool sizes and ex-situ analysis of the cross-sections that are obtained for different process parameters. Single and multi-layer builds and the size of the melt zone are also compared with the simulation findings.

The thesis is outlined as follows; in Chapter 2, a literature review has been carried out and how the processes and methods that are the subject of this thesis are captured in the literature are examined. Chapter 3 explains the experimental procedures and Chapter 4 describes the modeling approach. Chapter 5 and Chapter 6 include results & discussions, and conclusion, respectively.

2. LITERATURE REVIEW

2.1 Historical Background

The first term that can be accepted as the ancestor of this technology was mentioned for the first time in the 70s of a new technology called "Layer Manufacturing" (LM). LM differs from the manufacturing methods known until that day and will cause significant effects in the future. The key idea of this technique was creating a part geometry with high freedom in terms of geometric complexity and based on the principle of building layers on top of each other.

By 1984, the technology called "Lithography" was invented, and this development is regarded as the most decisive starting point for AM. Following this development, other AM types have been developed to date. Initially, polymer-based materials were used, then metal-based materials were introduced with laser technology, that is similar to the method used today. While it was accepted that it started with the invention of "Stereolithography" by Chuck Hull in 1984, from the 70s to the end of the 90s, the LM term was used. LM is also referred to as Rapid Prototyping (RP) in the sources [2].

In the late 1980s, the RP technology for model and prototype development studies as the pioneering goal increased the needs in different industries, renewed the demands of manufacturing methods. With Industry 4.0, it has grown rapidly and significantly in recent years [3]. Today, AM, also popularly known as 3D printing (3DP), is attracting attention as one of the rapidly developing production technologies in the world [4], [5].

By the early 1990s, another important milestone for AM was Fused Deposition Modeling (FDM), which laid the foundation for developing 3DP. Also, two other new AM technologies, namely Solid Ground Curing (SGC) and Laminated Object Fabrication (LOM) were commercialized. While FDM is based on the logic of extruding thermoplastic materials in filament form to create parts layer by layer, it is still used in many sectors to meet the RP need. SGC has the principle of using an ultraviolet (UV)-sensitive liquid polymer material and solidifying all layers in one pass by filling UV light from masks created with electrostatic toner on a glass plate. LOM uses sheet materials that are glued and cut with the help of a digitally guided laser. Selective Laser Sintering (SLS), which can be considered the starting

point of today's powder bed systems, was used for the first time in 1992. Using the heat generated by the laser source, SLS sinters powder materials to each other for selectively determining areas with Computer Aided Design (CAD) geometry for every layer [6].

2.2 Metal Additive Manufacturing

Metal AM methods, including DED, which is the focus of this study, are currently the most preferred used methods for functional parts in today's world. Additive Manufacturing is an up-and-coming manufacturing technology developing against the traditional subtractive manufacturing methods of material subtraction known today.

The parts build layer by layer using AM have many advantages and are preferred over subtractive methods. Underlying significant prominent benefits of AM technologies for users, when compared with conventional methods that draw attention in the industry, are; cost reduction on the parts that involve geometrical complexities for subtractive manufacturing, adaptive design and development for existing casting, and forging designs of parts for to reach conformance and required updates, and flexibility in production design by making it achievable to print complex geometries such as inner holes, thin walls, unique manifold geometries in fewer process steps like removing costly multiple-step and costly tooling and casting from manufacturing [7], [8]. Weight reduction will be another chief point where AM will be superior in parts needed and suitable to meet this design requirement. By designing the required features within the part (i.e., inner features) in the structure built layer by layer and providing the topology, AM will be much more helpful than milling, casting, and forging manufacturing processes in terms of weight reduction [9].

Besides, metal AM methods have gained great importance in different sectors, and their usage areas are becoming more and more common. Some of the major industries using AM stand out as; aviation and aerospace, automotive, medical, defense and energy, because of the advantages described above compared to traditional production methods and the benefits it provides to the user. Using metal AM is mostly seen in the aviation and medical sectors today. The major reason for this is for aviation: Needs a machine like an aircraft engine, which has very high complexity and high added value, requiring many components and assembly, needs the same high complexity from manufacturing processes. AM is useful here, thanks to the capabilities mentioned above. When we look at the medical and health sector,

which is another sector where AM is highly preferred, unique pieces are specially developed and specially designed according to the patient's size and requirements, such as the knee, hip implants, components developed for the mouth, and jaw disorders. [11], [12], [15] - [20].

For DED method specifically, areas of use in different sectors, by evaluating the process in line with its application purpose; manufacturing of parts, adding a feature on a manufactured part, and repairing a damaged part can be examined under 3 headings. In these sectors, especially in the aviation industry and mold manufacturing, high-cost and complex parts that have long periods of use and show different wear and tear conditions in this period can be repaired with DED applications with almost no geometric limitation, then they are ready for reuse in a very short time with conventional processes. Similarly, when additional details need to be added to the structures with complex geometries that have been produced before, it is possible to develop parts in a way that no other method will allow by adding element.

In another area of use, DED methods provide important possibilities to produce large-sized parts according to the current limitations of Powder Bed Fusion systems. Used in defense and aviation; the production of structural parts such as lightened bodies, engine parts such as combustion chambers with conventional methods, and the production of raw materials of larger sizes than the parts comprise shaping the raw materials in a long time with many different processing methods. High number of different equipment usage;Using large labor force, loss of time, increasing costs, and to give its final shape, up to 80% of raw materials are transformed into waste. Especially with the WAAM method, the rough production of parts with complex geometries can be completed with a single equipment, the buy-to-fly ratio is increased and thus material loss can be minimized.

However, besides its advantages, the metal additive manufacturing process also has some disadvantages. There are still some constraints today to provide the desired technical and financial benefit from metal AM. These limits should be improved so that the process can have wider use [10]. An example of these is that if the part that will still be produced with metal AM will not be produced in more than a certain number of batches and will be in a low number - or even a single piece - the cost will be higher compared to the traditional methods. If continuing to produce with metal AM and designing a part according to metal AM is included in the production plan, to turn to a high-complexity part design and continue with a

design that includes part customization in order to make it a cost-effective alternative, as shown in Figure 2-1 [10] seems logical for the current structure of the industry.

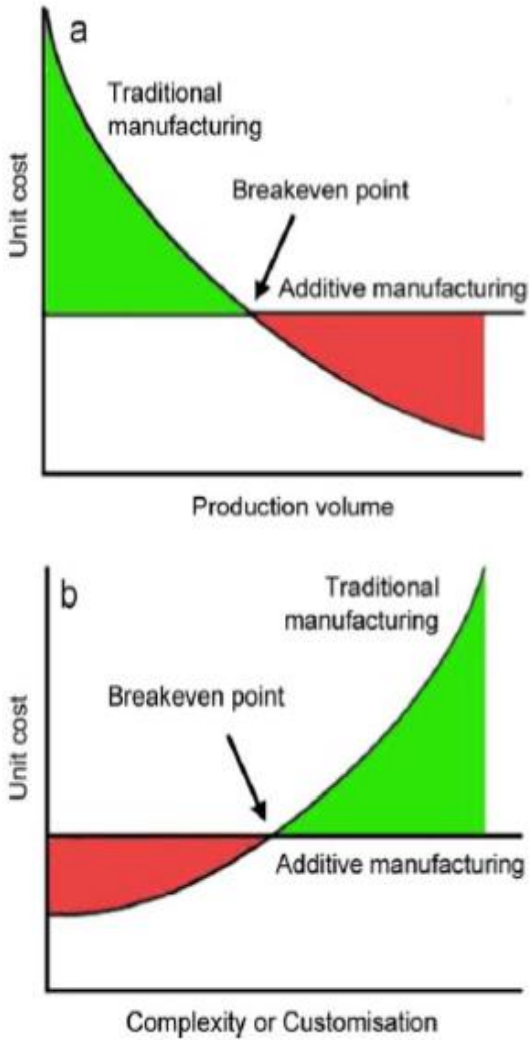

Figure 2-1 Breakeven point for unit cost – comparison of metal additive manufacturing and traditional manufacturing methods [10].

As explained in 2.2.1 and 2.2.2, metal AM methods can be divided into two categories to handle the metal material. These are powder bed systems and material feed systems. These systems can also be examined in subtitles within themselves because the heat source can be different. Table 2-1 represents the metal AM classification with commonly used commercial names due to manufacturer's trademarking and patent related trading name [11].

Table 2-1 Classification of metal additive manufacturing (AM) methods .

Technology	**Distinctive Feature**	**Commercial Name**	**Platform Manufacturer**
Powder Bed Fusion (PBF)	Laser Beam Energy Source	Direct Metal Laser Sintering (DMLS)	• EOS
		Selective Laser Melting (SLM)	• DMG Mori • SLM Solutions • Renishaw • Realizer
		Laser Metal Fusion (LMF)	• Sisma Group
		Direct Metal Production (DMP)	• 3D Systems
		Direct Metal Laser Melting (DMLM)	• Concept Laser
	Electron Beam Energy Source	Electron Beam Melting (EBM)	• ARCAM
Directed Energy Deposition (DED)	Powder Based Feedstock	Laser Cladding (LC)	• DMG Mori
		Direct Metal Deposition (DMD)	• POM
		Laser Engineer Net Shaping (LENS)	• Optomec
		Laser Deposition	• Huffman • Trumpf
	Wire Based Feedstock	Electron Beam Direct Melting (EBDM)	• Sciaky

2.2.1 Metal Powder Bed Systems

Inside the build chamber with inert shield gas protection (Argon or Nitrogen), a powder bed is created with a pre-determined layer thickness on the horizontal axis using the recoater blade to spread metal powder on the substrate homogeneously. Electron or laser beam energy source fuses the metal powders by melting them together with localized heat input by energizing the metal powder to have 2-dimensional cross-sectional areas on the powder bed. Additional metal powder is laid throughout the work area by the recoater blade once each layer is finished again, as much as layer thickness for the upcoming layer. The process results in the 2D cross-sections in the layers overlapping on top of each other to form a solid 3D component, resulting in the designed part [1], [12], [13]. Metal powder bed systems are examined under two main headings. The first one is the Powder Bed Fusion (PBF) method, which uses a laser beam as an energy source. The method is also known as Direct Metal Laser Melting (DMLM) and Selective Laser Melting (SLM) because of the nomenclatures patented by different companies at different times. Another method is the electron beam as an energy source known as Electron Beam Melting (EBM).

2.2.2 Metal Material Feed Systems

Powder bed metal AM equipment and machines, which are currently widely used in industry and academia, limit the part sizes that can be produced with a certain build chamber constraint. Therefore, PBF systems cannot meet the requirements, especially for the rapid manufacture needs of relatively large sized parts. The production of larger-sized metal parts with AM according to the needs of different sectors stands out and is important. DED method is an important opportunity to manufacture large-sized parts with a single manufacturing equipment by minimizing material loss as much as possible, where multiple different conventional manufacturing methods are used together and can be completed in long cycle times.

AM metal material feed systems, popularly known as DED, can be examined under two headings because of the type of feedstock material used and the type of energy source used as heat input for welding the substrate and creating the melt pool. Current DED systems typically operate in an environment under an inert shield gas (Argon or Nitrogen) for non-reactive materials, with a concentrated energy source (laser or electron beam) and a metal feedstock stream (powder or wire), which intersect at a common focal point generated by

closed-loop laser optic and mirror systems of the machine through a coaxial deposition. The energy density produced by the energy source used at a certain point causes the formation of a melt pool by melting the metal powder raw materials in and around that are in an area can affect due to heat generation (melt zone) [14]. This process is repeated until creating a solid 3D component [15], [16].

Among DED methods, powder-fed and wire-fed systems are more commonly preferred in production lines compared to other raw material feeding methods. Both feeding methods have different strengths and weaknesses, and the requirements specific to the target product and part to be produced play an important role in determining the method to be used and are determined by the user. When compared them in each other, powder-fed systems are more helpful in tolerance accuracy of parts that require high dimensional precision and low heat input. However, wire-fed systems are more helpful than powder-fed systems in terms of large part size, volumetric efficiency, and deposition rate.

The biggest difference of DED from PBF, which are accepted as the main two categories for metal AM, when we look at it in this sense, in fact, in the DED method, instead of melting a powder in a bed, the focused energy beam builds the material into a molten pool on the substrate surface with a powder or wire. Figure 2-2 [14] shows the categorization of DED method that is available in the market.

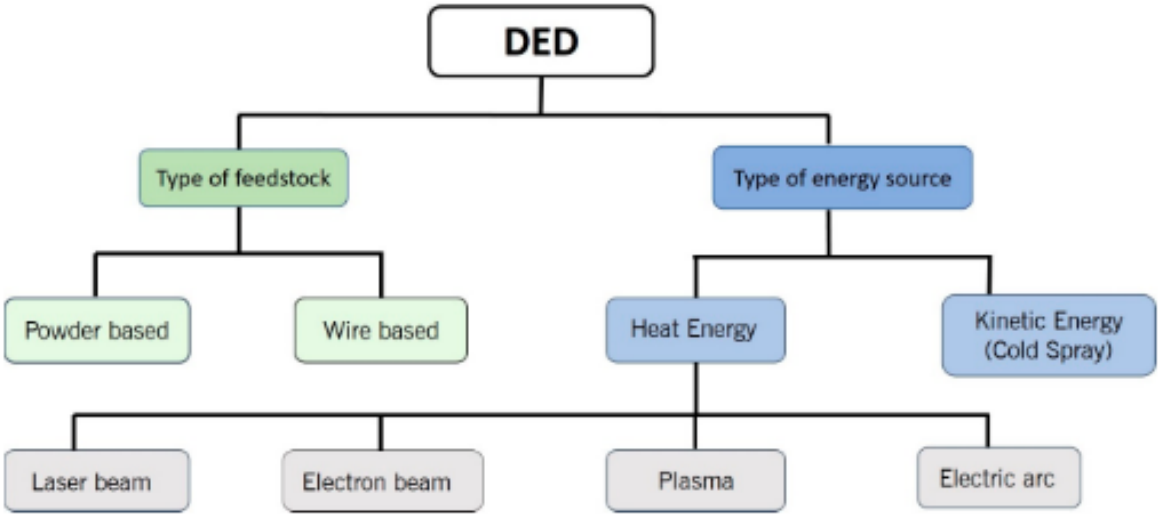

Figure 2-2 Classification of Directed Energy Deposition (DED) Systems [14].

DED technology with its acronyms also known as Laser Metal Deposition (LMD), Directed Metal Deposition (DMD), Laser Cladding (LC), and Laser Engineered Net Shaping (LENS™). Figure 2-3 shows the schematic briefly describing the DED method. When technology first developed, while metal wire-fed methods were used more widely, with the progress and developments, the most preferred options are now in favor of powder-fed laser energy sources in the industry. There are two predominant types of systems on the market. In the first one, the workpiece remains stationary, and the deposition head of the laser and material feed nozzle moves across the scanning path. In the second option, the deposition nozzle remains stationary, and the workpiece moves in different axes depend on machine capabilities[1]. Besides these, hybrid machines, which combine subtractive and additive manufacturing for high-level precision and gathering processes to decrease iterations and the number of post-process steps after AM, in which the manufacturing processes in this thesis are carried out, have been developed and used recently.

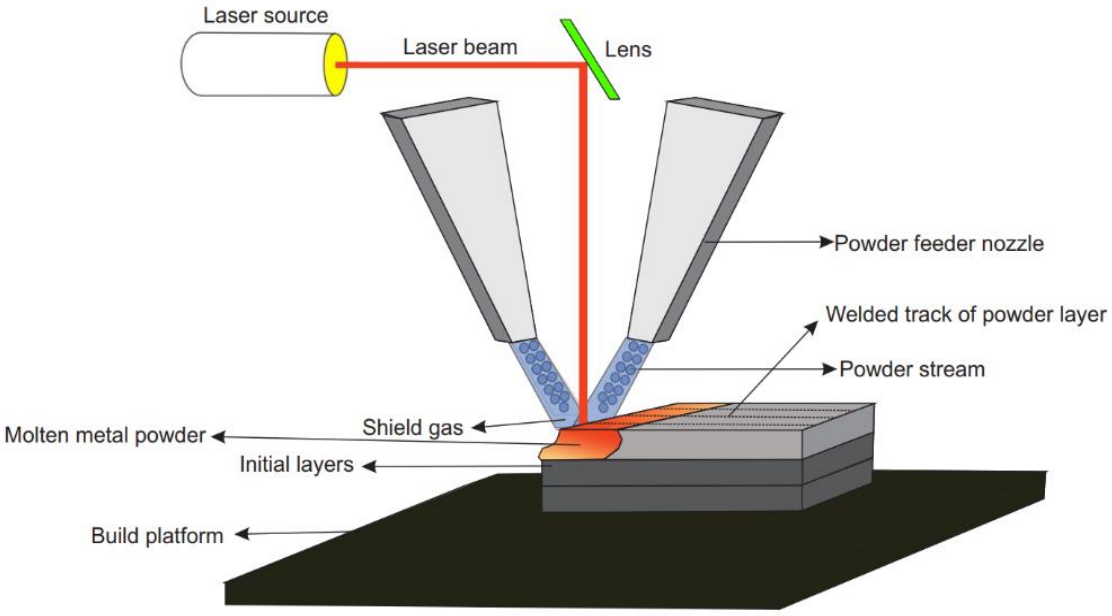

Figure 2-3 Schematic of powder-fed metal feedstock DED process.

2.2.3 Comparison of Directed Energy Deposition and Powder Bed Fusion

When we compare the DED and PBF processes, which are the two most preferred and most popular metal additive manufacturing methods among technologies, both processes have distinct advantages over each other. Even though they are under the same manufacturing technology, they have many purposes of use. DED operation offers several advantages when trying to reach near-net-shape. For example, metal parts with large geometries in terms of build volume for the build platform of PBF machines and cannot exceed geometric boundaries can be produced with the DED method [17]. The higher deposition (feed) rates of the DED process (5-30 g / min) compared to PBF (2-3 g / min) also help to produce large parts quicker than powder bed systems. One of the unique advantages that DED offers against PBF is repair capabilities of the process (i.e., Adding metal material for components due to damage or wear), regeneration, and coating of parts can only be done by the DED process among possible AM methods [18]. Hybrid systems that combine traditional subtractive and AM technologies often choose to combine DED with their solutions, rather than PBF, to take advantage of higher building speed and deposition rate [19], [20]. Although the DED process is faster than the PBF because of its ability to achieve higher feed rates and scanning speeds, it has lower geometric tolerances than the PBF process. After the DED process is completed, it is often combined with traditional subtractive methods such as 3-axis or 5-axis milling to achieve the desired geometric requirements while it may also need post-processes to improve its specifications in terms of surface quality such as surface roughness and hardness [19], [20]. Figure 2-4 [21] shows an example of additively manufactured parts with the DED method to be used in the aviation industry.

Figure 2-4 First DED AM structural airplane component - Boeing 787 Dreamliner.

2.2.4 Challenges in Additive Manufacturing

Besides all the great potential and good advantages of metal AM for today and the future, it also includes some problems and obstacles that have not yet been resolved in the process and affects the condition of the parts while resulting in lower accuracy and repeatability of the manufactured parts since it cannot capture enough sustainability as subtractive manufacturing methods.

Metal AM continues to grow and develop thanks to the notifications used with studies and research that are still being done now and for the future. There are good advantages that are potentially and currently available. However, as it is frequently referenced in the literature, it also contains a few setbacks. The occurrence of defects such as voids and porosities is frequently observed in metal AM parts as one of them. This problem cannot occur because of geometrical constraints only of the designs of the specific parts and cannot always resolve with design updates with Design for Additive Manufacturing (DfAM). These defects usually generate inside of the manufactured parts as pores, gas entrapments, and even keyholing phenomenon, while these porosities can also be observed very close to and on surfaces of parts. Valid selection and optimization of process parameters for additively manufactured parts are currently an ongoing research topic, with the research of reviewing the AM processes for the parts with unique characteristics such as bulk, contours, and overhang structures and trying to prevent possible errors. They are observed as an essential reason in many critical aspects, from the surface quality of the part, mechanical properties, crack formation, and even fatigue behavior [16], [22].

Another significant problem for metal AM is the residual stresses that occur during the process[14], [23], [24]. The primary and most crucial reason for residual stress during AM is the thermal gradients formed between the comparatively colder substrate that the desired part geometry is built and the deposited metal powder layer simultaneously with heat input [13], [25]. The primary reason for the development of thermal gradients during the process is because of the creation of melt pool geometry by the laser for powder penetration are very small compared to the dimensions of the substrate on which the process is carried out or the layer that has already been processed and solidified. A small-sized melt pool, although which is important for keeping the values in tolerance limits and surface quality at a high level, reaches very high-temperature values where the laser and the substrate or the previous layer

interact with each other. However, temperature differences occur with other regions outside the melt zone and remain at lower temperatures compared to the melt zone, which causes the large thermal gradients. Repetitive dynamic thermal cycles as subsequent heating and cooling occur in part during the process are known as reasons for the formation of unwanted residual stress in AM [26]–[28]. Besides this information, it has been observed that residual stresses that will occur in AM parts can have a fatal effect on the fatigue life of the part and also on its static mechanical properties [29]. The successive heating and cooling cycles that occur with the high heat input given to the part cause tensile-type residual stresses in part. These tensile stresses can adversely affect the fatigue life by providing an additional driving force for cracks and even growth and progress. They can cause the part to fail earlier than the calculated part life [30].

The residual stresses that occur may eventually result in distortion of the part and the substrate, since the heat input affects both. The resulting residual stresses will affect the part and the substrate to which it is welded, which means an obstacle for the additively manufactured product to finally become scrap and waste [28], [31].

When we look at the mentioned problems and undesired setbacks; because of repetitive heating and cooling cycles, the formation of thermal gradients that occur as explained and distortion with residual stresses on the part prevents the part from meeting the target design criteria while losing its functional capabilities and the resulting loss of tolerances. It may even be unsuccessful and may cause scraping.

These problems, which are mentioned in the current conditions, are tried to be addressed by using an experiment-based trial-and-error approach with consecutive additively manufactured samples must be produced, with a need to repeat many times and may require many iterations depending on the complexity of the part, to reach the intended aim. This method can be expensive, together with the machine, raw material, and labor requirements used for AM. Besides its time-consuming manner, it provides a very low level of information on thermal history, temperature distribution, melt pool characteristics, geometry, and dimensions, followed by thermal gradients, distortions, and residual stress that will be simulated with a thermal model. Because changes that may appear minor but have a significant impact can occur before the part is manufactured or during manufacturing, which may have the potential

to occur, in this respect, there is a need to develop a model that can replace trial and error and save time and money.

2.3 Prior Modeling Studies

In the metal additive manufacturing process, studies have been carried to understand better and improve the manufacturing process mechanism starting from the previous years on the occurrence of these significant matters mentioned in many sources, such as the above examples. By investigating the process based on simulating the process with FEM, it is tried to develop the methods that are very important in the calculation of such as temperature field, residual stresses and distortions in metal additive manufacturing, the effect of the manufacturing process on the quality of the part produced.

Computer simulations are beneficial to reduce high costs by eliminating the time-consuming trial and error of experimental methods and identifying the process parameters for the material properties [32], [33]. Studies in modeling are carried out to research and understand physical relationships numerically and to minimize the cost and time required for the process. At the beginning of the studies for the DED process, 2D numerical models with lower complexity were studied. Later, interest in 3D modeling studies increased to reflect the complexity of the process more accurately and more successfully. Using FEM was preferred to simulate metal material deposition with a developed model [34], [35].

In the DED process, many process parameters must be defined by the user. It must be controlled and represented in the simulation, which is also the AM process environment's return. Using methods such as FEM enables users to simulate and estimate these parameters with the best possible convergence to reality. Understanding the temperature and distribution of the process parameters by the heat input generated during AM and explaining the formation of metal material deposition by modeling the melt pool's physical representation plays a critical role in understanding how to control the process and essential process parameters and making the improvements [36], [37].

As mentioned, the importance and use of FE tools in process modeling have been emphasized in the literature. In numerical modeling, the key steps can be explained sequentially as preprocess, process, and post-process. Some of the preprocess include model geometry,

boundary conditions, initial conditions, and material properties. With processing, the governing equation and solution are examined [38].

When it is desired to examine the historical progress of modeling studies for DED in the literature, it would be meaningful to start from the welding process modeling. The process shows many similarities and sheds light on the studies for DED modeling.

2.3.1 Welding Process Simulations

Finite Element Method process models have significant similarities with welding model and process modeling methods developed and used for metal AM are very similar to welding modeling methods in the literature [39], [40] and even in the literature some of these welding process modeling methods have also been used for metal AM methods [23], [41].

Using FEM to predict the thermal gradient structure that occurs in AM, the effect of the heat zone, distortion and residual stress is due to the previous studies in the literature on the occurrence of similar situations in the welding process. The welding process has many similarities with the metal AM and especially with the DED method. As mentioned in the previous titles, in the welding process, a heat source can be defined as the melting of the material on a workpiece that can cool and solidify after laser deposition of metal material. As a result of this process, just like metal AM, thermal gradients are created due to the heating and cooling cycles, resulting in undesirable residual stresses in the part and often distortion of the part [42], [43].

2.3.2 Thermal Modeling for Directed Energy Deposition Process Simulations

Some steps must be followed to reflect the process of an additively manufactured part accurately. First, it is vital to represent and model the thermal response accurately. To make sense of deposited metal material formation, it is first necessary to understand the melting process. For the metal material to be added, the substrate where the deposition will be carried out must first reach the melting point. Therefore, the formation of the melt pool between these two materials when they interact with each other (the same or different materials may have been used) during the material deposition is critical and should be understood correctly. To understand the melt pool, one can examine different variants.

These can be melt-pool dimensions, shape, phase state, and temperature values at specific coordinates of the heat-affected zone (HAZ). Various studies were conducted to examine some critical parameters used in the process of thermal history. In the study that models the heat transfer in 3D for DED, laser power, scanning speed, beam diameter, and mass flow rate were used to calculate the amount of energy generated. As a result of the study, it was stated that the increases in laser scanning speed cause growth in the liquid-solid interface of the melt pool and therefore increase the cooling rate between solidification and liquidus temperatures [44].

In the studies for modeling with the FE, first among the research in the literature, some studies examine the thermal behavior of the process and its effect on product quality [38]. Both numerically modeled and experimentally investigated the thermal behavior during the DED process for AISI 316 stainless steel material. They developed FEM to predict and get temperature distribution with thermal gradients in part with conducted experiments. As a result of their study, it was reported that the temperatures around the melt pool area decreased and increased radically and gradually decreased with increasing distance to the melt pool. [45]. Peyre *et al.* developed an analytical model primarily for calculating the powder temperature and tried to estimate the geometry of the modeled thin wall structures with a combined numerical and analytical modeling using a discretization of the physical interaction field and performed a FEM on the developed model [46]. Fu *et al* have developed a model in DED that aims to predict the temperature distribution that occurs during the process. As a result of the study, if the deposited metal powder and the substrate material generate lower thermal conductivity and expansion values, the residual stresses due to thermal gradients will be lower. As a result of the conclusions made from the study, they reported that increases in the laser power and scanning speed of the process parameters might lead to higher peak temperatures, increasing residual stresses [47]. Batut *et al.*, in their work on DED in two different methods, analytical and numerical FEM models, have done their research to predict the temperature change that occurs during the process. In the study supported by experiments, the target output was to estimate the temperature gradient, cooling rate, and melt pool geometry accurately. The study results reported that the analytical method provided an effective and accurate method to understand the effect on the temperature of the part during laser deposition with reduced computational cost compared to the numerical method [48].

Kelly and Kampe conducted a study modeling the process to understand the microstructural evolution in the laser deposition of Ti-6Al-4V materials. A numerical thermal model based on the implicit finite-difference technique was developed for this. To observe the effect of laser scanning speed on thermal history, one of the process parameters, they set up experiments with single-line structures [49]. Gockel *et al.* conducted a 2D FEM study suggesting that the relationships between the melt pool geometry for Ti-6Al-4V material and microstructure control such as beta grain size are independent of the deposition geometry and tested these studies with experimental verifications on the process of wire feed material deposition [50]. Gouge *et al.* developed a method for including an improved thermal convection input in the analysis when modeling the DED process in FEM and validated their experiments and work [51]. Gan *et al.* developed a model to simulate heat transfer, fluid flow, and solidification of cobalt-based alloy material on steel substrate and suggested solidification properties such as thermal gradients, solidification, growth, and cooling rates which can be obtained by transient thermal distribution [52]. Ren *et al.* developed a thermal history analysis with FEM to observe the effect of differing hatch patterns, one of the critical process parameters in AM, for prediction of thermal field and to establish a correlation between minimum distortion and optimum scanning pattern, created a thermal field-based evaluation method and verified with a rectangular-shaped deposition on with several scanning patterns [53], while Ju *et al.,* focused on the generation of a FE thermal simulation to see the effect of scanning speed on the dilution rate on the parts manufactured by designing a model for 304 stainless steel materials with the laser deposition process, testing of finite element simulation and establishing the temperature field with FEM [54].

2.3.3 Thermomechanical Modeling for Direct Energy Deposition Process Simulations

In 2.3.2, it is explained why thermal metal AM models are needed and how solutions are sought in the literature. Thermal gradients caused by the high energy input cause thermal expansion and contraction in part cyclical, resulting in residual stresses and distortion because of the situation.

For this reason, the modeling process has been further developed as a common practice to treat the metal AM process as a thermomechanical coupled boundary value problem to detect residual stresses and geometric distortions in part. In their study, Ding *et al.* tried to make sense of the stress development caused by thermal cycles during Wire Arc Additive

Manufacturing (WAAM) by modeling a transient thermomechanical FE model. They concluded that the highest temperatures occurring during manufacturing were the most critical factor determining the residual stress of this point. Thanks to this data, they created a FEM that they claimed to be efficient and showed that their models provide high gains in computation time compared to traditional transient thermomechanical approaches and experiments [24]. As a result of the thermomechanical analysis and experiments they developed for their work to find the optimized path planning for DED, Ren *et al.* resulted that it was caused by the non-uniform stress distribution in the axis's direction. However, they reported that when laser path planning is applied in terms of width, more homogeneous stress distribution is observed in the x-axis regarding the y-axis. Therefore less distortion occurs in the x-axis accordingly [31]. Liang *et al.* proposed a modified inherent strain model in their study. The data obtained from the analysis were used in the static equilibrium analysis to reveal the residual distortion of the AM part. To verify the model they developed, they carried out experiments with the DED process, proved the proposed model's accuracy, and showed that it could decrease 80 percent in computational efficiency thanks to the method they used [35]. In the thermomechanical model they developed for DED, Lu *et al.* examined complex geometries, one of the common problems of modeling studies, and deposited 44 layers of rectangular and S-shaped geometries as examples to model as complex geometries. Also, in their work, different process parameters were evaluated to examine their sensitivity to the process evaluation while also trying different substrate preheating strategies before initiating DED to be an example in classifying residual stress and its resulting distortions [55]. In the study of Stender *et al.*, the experiments performed with the thermomechanical model of the DED process developed for part-length geometries were compared. It shows that the experimentally measured in-situ thermal measurements and local hardness distribution in the part and plastic strain accumulation were compatible with the general trends [56]. A three-dimensional thermo-elastic-plastic model has been developed by Yang *et al.* using FEM to simulate thermomechanical process analysis for Ti-6Al-4V material used in the DED process. To validate the model proposed in this study, a comparison of the simulated distortion of the lower surface of a thin substrate regarding both magnitude and distribution map with experimental measurements performed using a 3D laser scanner was performed. Both quasi-static and dynamic simulations were performed and mechanical comparisons were made among each other [57]. For Ti-6Al-4V material, a thermo-mechanical model was by Cao *et al.* to examine the distortion and residual stress in the DED process and single and multiple layer parts were investigated. Model validation is achieved by comparing the estimated residual

elastic strains with the measured values obtained by neutron diffraction for the multi-layer part. For comparison with simulation, the distortion values occurring in the substrate were measured, and the effect of pre-manufacturing preheating of substrate on distortion and residual stress distribution, which was thought to have a significant effect on the process, was then examined using the validated model. It is stated from the results obtained that preheating at least twice is an effective way to reduce both distortion and residual stresses [58].

These models, which deal with the solution of the thermo-mechanical coupled boundary value problem, basically contain three different disciplines on their own. The thermal problem itself involves getting the temperature distribution within the boundary conditions and the heat input to focus on its solution, defined within the model by material properties and constituent laws. When we look at the material's physical properties, they can be found after the thermal solution since they are open to change with temperature. The mechanical equilibrium problem can be expressed as the balance of internal forces with accepting the static problem. After solving the mechanical problem, displacements can be found. Thermo-mechanical process simulation will be achieved by a subsequent solution to the thermal problem, identifying the material, and finally, the mechanical problem.

2.4 In-situ Process Monitoring

In the literature developed for AM, specifically for DED process, starting from the pioneering welding for DED, both thermal and thermo-mechanical studies have been examined in detail in previous titles. It is precious to support and validate these methods, which aim to represent the manufacturing process in the best way and to simulate the user in the most appropriate way and to save time and money, with experiments during the development and improvement phase and can be a part of the modeling process in a concurrent manner.

For this reason, besides the examination of modeling supported by experiments, the tools that should validate these models with experiments were also considered as part of the literature review. During manufacturing, in situ measurement methods are used to collect the data of the process trying to be obtained in the model with the user's measurement options and compare the collected data with the model by processing.

During the DED process, for the developed analytical or numerical model, in situ temperature monitoring can be used to observe thermal cycles between layers during the built of layers

during manufacturing or in the interaction of the melt pool during the first layer with the substrate and by the analysis of this data, it can also verify the thermal models [46]. Many commercial DED platforms have already a temperature monitoring system today integrated into the machine's closed-loop integrated system with its data acquisition infrastructure [11]. In situ measurements can be divided into contact measurements and contactless measurements and can be selected by the user depending on the quantity and quality of the collected data . One of the most common options, thermocouples, is used to monitor the temperature of the substrate, which is cyclically undergoing heating and cooling phases by heat input generated by energy source during deposition. Thermocouples in certain parts of the substrate should be placed as much as possible in areas where heat accumulates during the part build and where temperature monitoring is possible. In this way, custom-designed substrates can be used, or substrates with drilled holes as many as where the thermocouple measurement sensor can be placed [59]–[61]. Contactless measurement instruments are frequently used in the literature with their different capabilities such as infra-red (IR) temperature sensors [62], [63], and pyrometers to access temperature data rather than only monitoring substrate template temperatures, by capturing generated temperature history of build parts with investigating melt pool and HAZ temperatures [18], [41], [64]. In custom-designed DED systems, IR temperature monitoring was used to ensure the desired temperatures to identify the best sample to nozzle working distance [65].

Besides observing temperature values, in situ measurements of distortion are among the monitoring methods in the literature. Various researchers have designed their experiments with a laser displacement sensor (LDS) used for the free end of the substrate, fixed from the other side with various methods such as a clamp, to measure distortion in the z-direction of the part and the substrate. This design may require changes to the setup of AM machine, as well as unique fixture design depending on the machine and part design [25], [59], [66].

3. EXPERIMENTAL WORK

3.1 Outline

Directed Energy Deposition (DED) Additive Manufacturing (AM) experiments were performed in Sabancı University Integrated Manufacturing Center (SU-IMC) in Teknopark Istanbul. Experiments were conducted on Lasertec 65 3D device, shown in Figure 3-1, a 5-axis hybrid platform used for both additive and subtractive manufacturing, developed by Sauer GmbH / DMG MORI AG. The machine has equipped with a Coax 14 powder nozzle and a 1020 nm continuous-wave diode laser with a maximum laser power as the energy source of 2500 W. The laser melts the powder carried by Argon gas feed on the substrate during manufacturing.

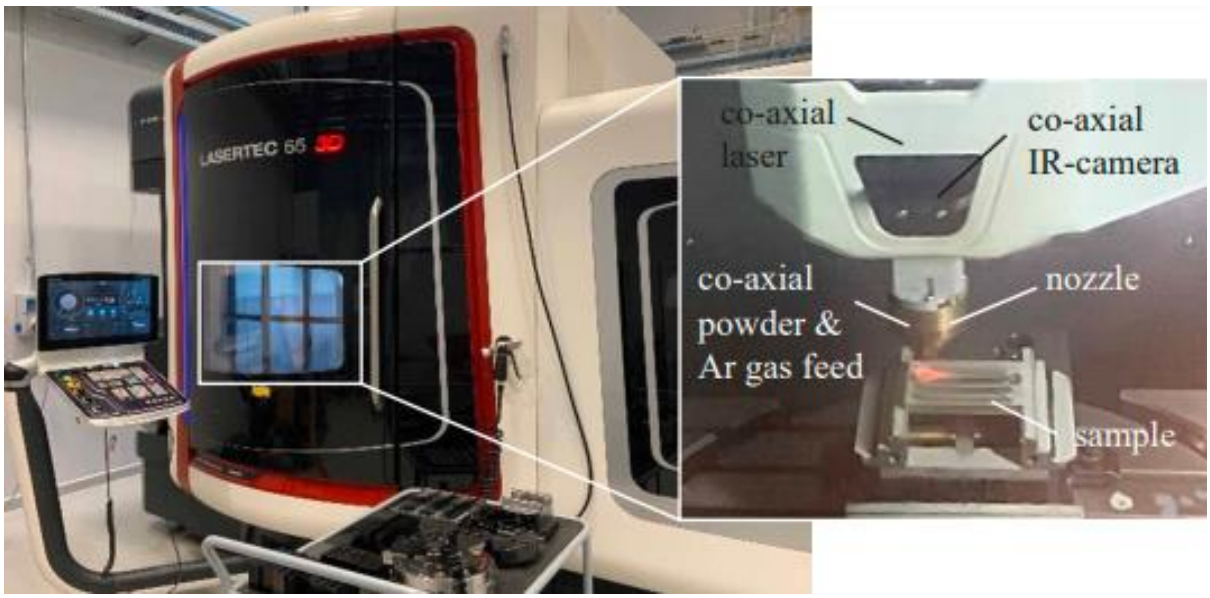

Figure 3-1 DMG MORI Lasertec 65 3D hybrid additive and subtractive manufacturing machine.

High-strength, corrosion-resistant nickel-chromium, Inconel 718 (IN718) metal gas atomized powder material used for deposition onto the laser focal spot as powder-fed raw material. For this, metal powder material, which is spherical and ranging in size from 45 to 90 μm was used. The chemical composition of IN718 is listed in Table 3-1.

Table 3-1 Chemical Composition of IN718 powder material / wt.%

Ni	Cr.	Fe	Nb	Mo	Ti	Al
Bal.	19	18	5	3	1	0.5

The substrate material was grade 316L stainless steel (SS 316L) metal material frequently used in industrial and academic studies as the substrate for AM applications. IN718 type metal powder material was built or deposited over the SS316L substrate. The dimensions of the substrate were 100 mm × 60 mm × 10 mm in length × width × thickness, respectively. Before parts are manufactured on a substrate, the parallelism of the substrate's top and bottom surfaces was measured to prevent any distortion and cleaned with the help of ethanol.

3.2 Setup and Experiments

Other machine and process parameters, which are explained in 3.2.1 and 3.2.2 below, except for the parameters planned in this study to examine the effect through experiments, were kept constant in both single-track and multi-layer deposited samples. Except for the parameters prepared for the experiment, varying between parts, all other parameters been constant throughout all experiments. Layer thickness, one of the critical process parameters, is not investigated as a varying process parameter set and kept constant as 0.45 mm for all layers. The value chosen is the AM machine manufacturer's recommendation of layer thickness value for IN718 thin-wall structures. Table 3-2 shows other machine-related process parameters.

Table 3-2 Machine related constant process parameters for single-track and multi-layer experiments.

Stand-off (Working) Distance [mm]	**Laser Spot (Top Head) Diameter in Focus [mm]**	**Powder Flow Rate [g/min]**	**Protective Gas Flow Rate [L/min]**	**Carrier Gas Flow Rate [L/min]**
13	3	15	5	6

3.2.1 Single-Track Builds

The deposition as single-tracks (also referred as single-layer, single-bead and laser clad in literature) with different process parameters was performed to examine the effect of the process parameters used during the additive manufacturing process on the melt pool geometry and behavior. The single-track dimensions were 80 mm × 3 mm × 0.45 mm for length × width × thickness, respectively. The single-track builds were manufactured by deposition of 3 single tracks on every three separate substrates resulting in 9 single-track builds. Figure 3-2 shows single-track depositions for various process parameters: scan speed such as 12.5 mm/s,16.7 mm/s, and 22 mm/s at three different laser power; 1500 W, 2000 W, and 2500 W, respectively. Table 3-3 shows laser power and scan speed as varying process parameter combinations that are used in experiments and simulations. Process parameters for laser power were selected by including the maximum power. The values chosen for the laser power and scan speed were chosen to consider the possibilities offered by the machine. In addition, to examine the effect of laser power and scan speed, a difference between values was tried to be created. However, it was aimed to prevent possible negativities caused by the capability of the process parameter rather than the desired situations by not exceeding extreme limits.

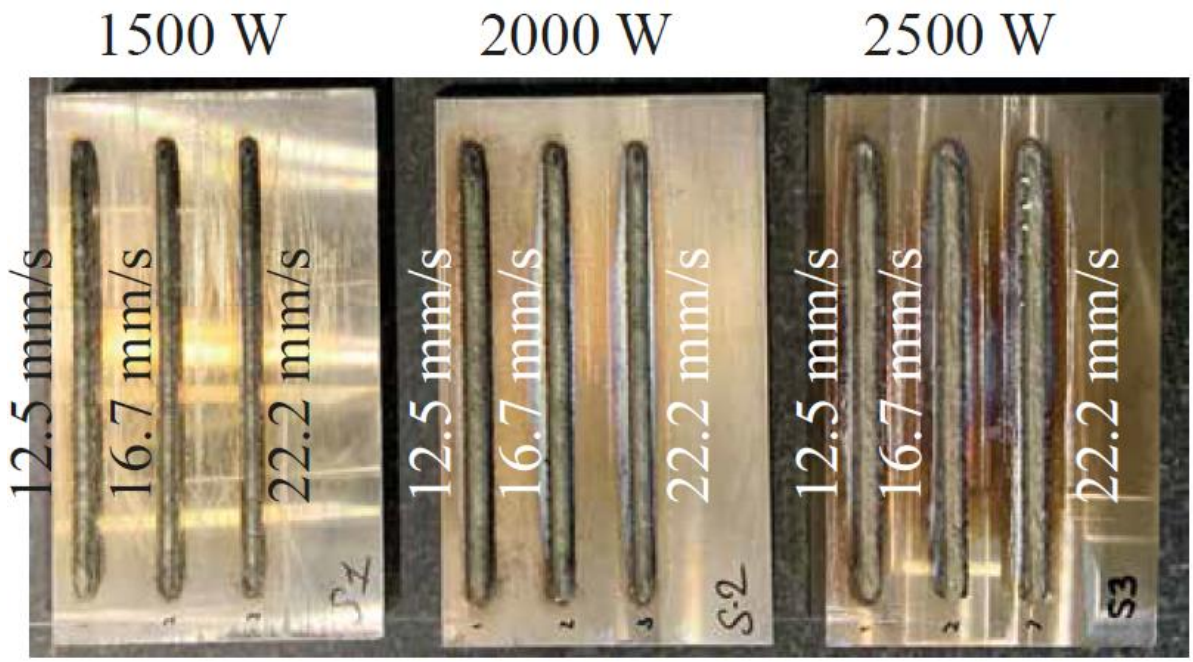

Figure 3-2 Single-track samples with different process parameters; laser power and scan speed.

Table 3-3 Different laser power and scan speeds as the process parameters for single-track builds

Laser Power [W]	Scan Speed [mm/s]
1500	12.5
1500	16.7
1500	22.2
2000	12.5
2000	16.7
2000	22.2
2500	12.5
2500	16.7
2500	22.2

3.2.2 Multi-Layer Builds

For the multi-layer experiments, the same machine setup used in the single-track experiments was established. All the multi-layer samples deposited consist of 8 layers. With the same design of experiment manner, samples with two different laser powers and three different scanning speeds were manufactured, resulting in 6 in total. The size of the substrate and the geometry of the deposited geometries remained the same, while laser power and scanning speed were analyzed as experiment process parameters. In the deposition of multi-layer samples on top of each other, instead of the IN718 metal powder material deposited on the substrate, the parameter sets seen in Table 3-3 are used because the formation of the same materials will be examined from the first layer until the completion of the geometry for consecutive layers, 8 in total. Figure 3-3 shows multi-layer depositions for various process parameters: scan speed such as 12.5 mm/s,16.7 mm/s, and 22 mm/s at two different laser power; 1500 W and 2500 W, respectively.

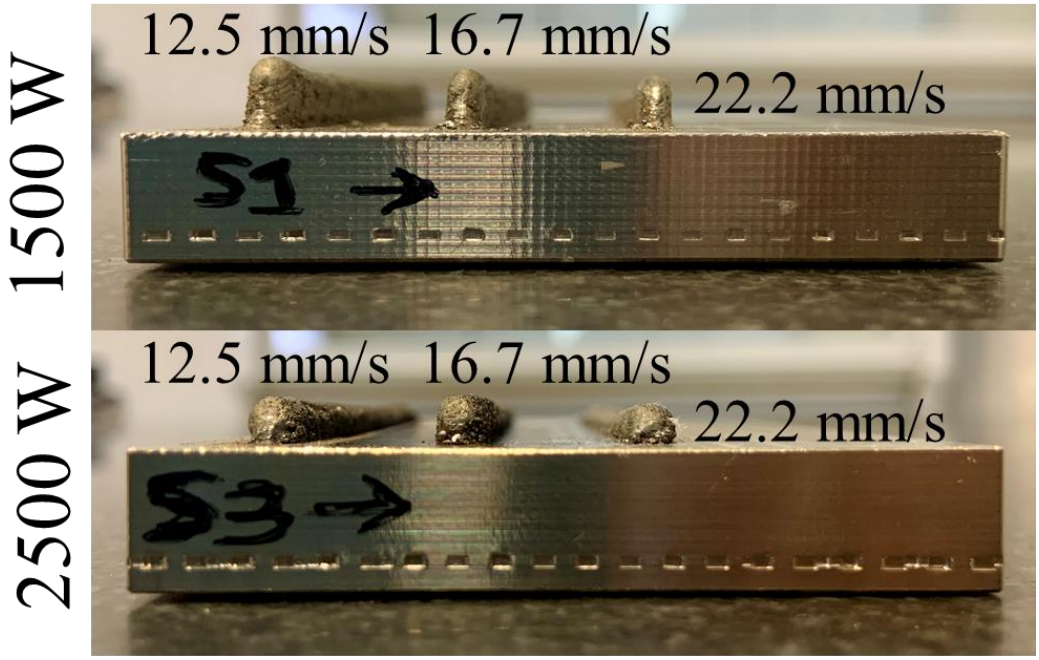

Figure 3-3 Multi-layer samples with different process parameters; laser power and scan speed.

Table 3-4 Different laser power and scan speeds as the process parameters for multi-layer builds.

Laser Power [W]	**Scan Speed [mm/s]**
1500	12.5
1500	16.7
1500	22.2
2500	12.5
2500	16.7
2500	22.2

3.3 Metallographic Sample Preparation

Metallographic sample preparations for ex-situ analysis of both single-track and multi-layer samples were completed following the same procedures. Optical microscopy (OM) analysis was performed on the cross-sections of samples after the study. Based on the coordinate system used during manufacturing, the sections taken perpendicular to the laser scanning direction (y-z plane) were chosen to observe the interactions of the deposited tracks between the substrate and the layers and to examine the melt pool dimensions. The samples were cut

using the abrasive water jet cutting in SU-IMC, and the deposited samples were left as remained on the substrates in the "as-build" condition, in 6 mm thick sections each. After cutting, all cross-sections were embedded in the resin. The mounted cross-sections were then wet-polished using up to 4000 grit SiC grinding papers. Next, cloth polishing was done using a 1μm aluminum-oxide suspension. A solution containing 40% HCl (hydrochloric acid), 30% CH3COOH (acetic acid), and 30% HNO3 (nitric acid) was prepared for chemical etching. The polished surfaces of the samples were etched in the prepared chemical solution for 15 seconds to reveal the melt pool geometry and microstructural properties. Imaging of the etched sample surfaces was carried out with the help of an optical microscope for single-track builds (Nikon LV100ND). For multi-layer builds, A Nikon SMZ800N stereomicroscope was used for OM because of the larger size of deposited 8 layers and to capture all necessary interested features for analysis. Geometric measurements such as height and width of the cross-sectional areas of deposited and substrate materials were determined using the OM analysis with measurement software ClemexVision. Figure 3-4 shows the state of samples after these preparation steps.

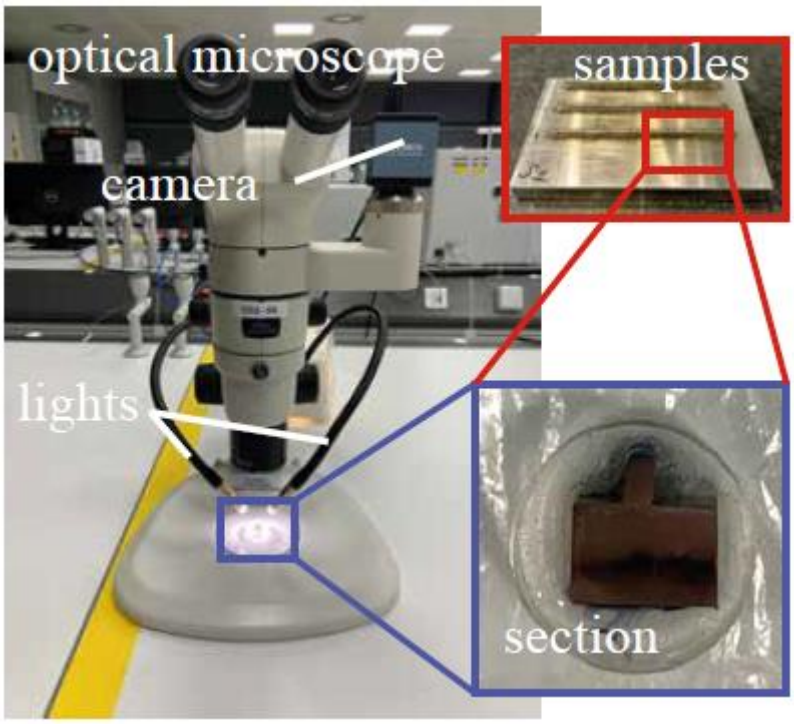

Figure 3-4 Sample preparation steps sectioning, polishing, and etching of the samples, and Nikon LV100ND optical microscope system that was used in the analysis.

3.4 In-situ Data Gathering and Image Processing

During the manufacturing, the heat input generated with the movement of the laser forms the melt pool with the powders coaxially deposited on the substrate or previous layer. An image process study has been carried out to calculate the size of the formed melt pool in terms of area and compare it with the developed simulation model. With this study, it is aimed to visualize the data and gain information knowledge about the melt pool taken from the device.

The process IR thermal camera, which is integrated with the laser head on the device, gives the outputs that enable analysis from the melt pool at the time of the experiment and the data presenting the temperature distribution. The process camera uses the light intensity values captured from the melt pool when the laser and the powder interact with each other and begin to lasing the substrate or the previously deposited layer. A calibration emitter that simulates predetermined temperature steps defined the correlation between light intensity and melt pool temperature. The reflection intensity from the local zone correlates to the melt pool intensity. If there is a high intensity within the melt pool, the reflection intensity is high as well. This results in not all bright spots coming from the zones of the melt pool led to a reflection. It depends on the angle of the beam reflected from the zone and captured successfully.

The in-situ generated data of the temperature distribution formed as frames can be collected. Here, how many frame data will be stored is at the user's discretion. For all the experiments in this study, one data was stored in every 20th frame. This results in information of 3 to 5 temperature distribution data per layer deposited. The most important reason for the different numbers of layers is the experiments at different scanning speeds, leading to a change in the increase or decrease in manufacturing time for each specific parameter set. These formed frames show the intensity distribution of the melt pool radiation. To extract the temperature distribution with this data, the created files must be scaled with the camera calibration file supplied by the device. This file contains values from two different columns. The first column shows the density values, while the second column corresponds to the temperature values. Each frame comprises 164 x 218 matrices, while each of them represents the pixels of the sensor of the camera of the device.

With these inputs, the author generated an image processing code in MATLAB® to analyze the locally occurring temperature distribution within melt pool. To calculate the number of pixels into mm², a calibration factor value is calculated. A flashlight is placed to see nozzle aperture (opening) as a bright circle in the camera image and stored this image using software called "Vimba Viewer" embedded inside the machine to calculate a calibration factor. With the help of the computer inside the machine, the camera is selected and can see images and/or an image stream. After that, nozzle opening is measured in mm using a caliper and measured the cross-section of the open circle in the camera image. Eqn. 2.1 describes the measurement for the area by using the described method above.

$$[9.5179\ x\ 10^{-4}]\ x\ \text{Number of pixels}\ (\text{mm}^2) = \text{Number of pixels in area}\ (\text{mm}^2) \quad (2.1)$$

With the code generated on MATLAB®, the calibration file and pixel values from each frame were scaled. To detect the melt pool on the temperature distribution image created, the device gave the temperature value of 1833 Kelvin as the upper limit of the color bar values. To estimate the size of the area in the elliptical geometry of the melt pool on the resulting image, the code prompts the user to select four different locations. These are:

- The origin points of the melt pool (Point A in Figure 3-5) from the threshold-colored boundary.
- The uppermost point of the melt pool (Point B in Figure 3-5) from the threshold-colored boundary.
- The lowermost point of the melt pool (Point C in Figure 3-5) from the threshold-colored boundary.
- The rightmost point of the melt pool (Point D in Figure 3-5) from the threshold-colored boundary.

With the point locations, the developed code calculates the ellipsoid area by using the minor and major axis values. As a result, the code generates an estimated value of melt pool area to the user. Figure 3-5 shows an example of the generated images from the developed image processing tool.

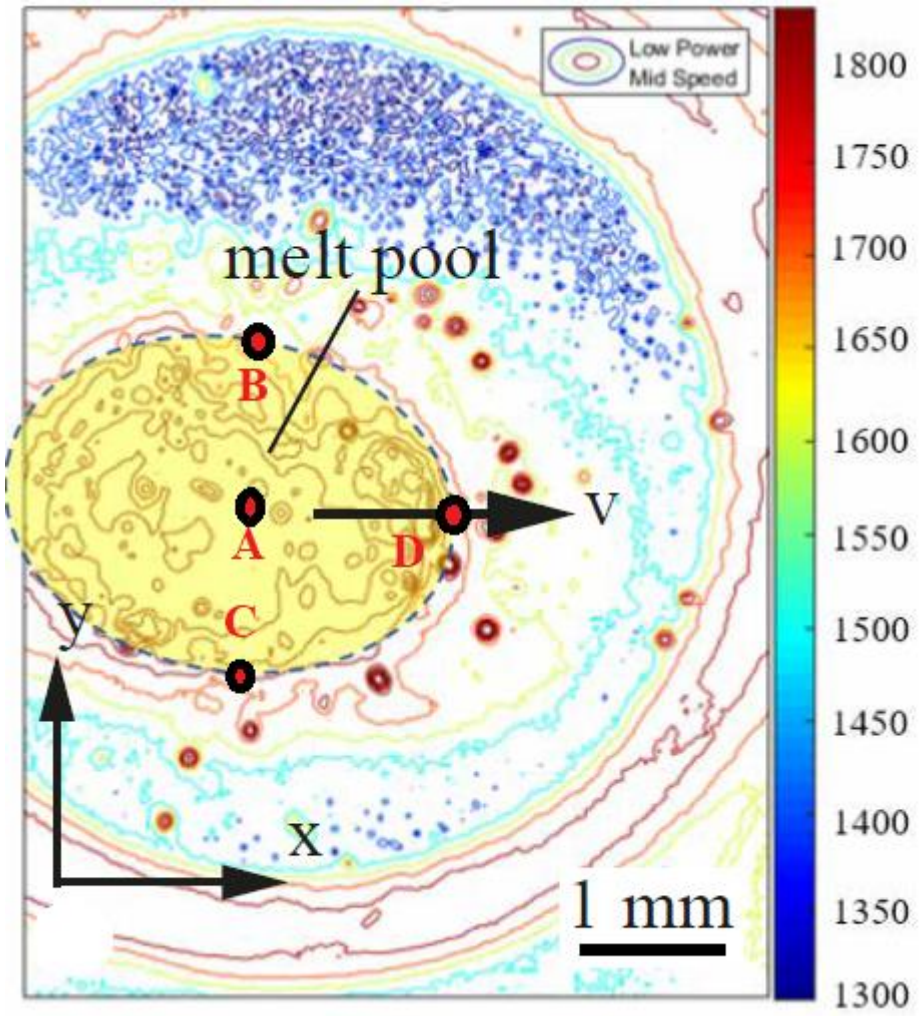

Figure 3-5 An example processed image output of melt pool area calculation by developed image processing code using in situ gathered data during manufacturing.

4. MODEL

4.1 Thermal Model

DED process is simulated by first solving the thermal history of the process using 3-dimensional (3D) transient thermal analysis. Using the governing transient heat transfer energy balance, a developed thermal model seeks the transient temperature field. Equation 4.1 represents the local energy balance of the material given as:

$$\rho C_p \frac{\partial T}{\partial t} = -\nabla.\ \mathrm{q}(x,t) + \dot{Q}(x,t) \tag{4.1}$$

where ρ is the material density, C_p is specific heat capacity, T is the temperature, q is the heat flux vector, t is the time, $\dot{Q}$ is the heat input and x is the relative reference coordinate.

For heat input, Goldak's double ellipsoid model is used, as shown in Equation 4.2. $\dot{Q}$ is the heat input per unit volume, P is the laser beam power, and η is the lumped efficiency factor while r_x, r_y, and r_z represent the laser spot radii in x, y, and z directions, respectively.

$$\dot{Q}(x,t) = \frac{6\eta\sqrt{3}P}{\pi\sqrt{\pi}r_x r_y r_z} \exp\left[-\left(\frac{3x^2}{r_x^2}\right)\left(-\frac{3y^2}{r_y^2}\right)\left(-\frac{3z^2}{r_z^2}\right)\right] \tag{4.2}$$

The heat flux vector, q, is computed using the temperature gradients using conductivity mapping, temperature-dependent thermal conductivity, k, as shown in Equation 4.3.

$$\mathrm{q}(x,t) = -k\nabla T \tag{4.3}$$

Heat loss through convection is integrated into the model for surfaces exposed to an open inert gas (Argon) pressurized environment. The corresponding heat transfer rate from the surfaces, $\dot{q}_{con}$, is calculated using an effective convection coefficient, h_{con} and ambient temperature T_{amb}, as shown in Equation 4.4. In the analysis carried out, the convection coefficient is 15 W/m^2K.

$$\dot{q}_{con}(x_s,t) = h_{con}(T - T_{amb}) \tag{4.4}$$

Radiative heat loss, $\dot{q}_{rad}$, from the exposed surfaces is computed using Equation 4.5, where ∈ is the emissivity and K_B is the Stefan-Boltzmann constant.

$$\dot{q}_{rad}(x_s, t) = K_B \in (T_-^4 T_{amb}^4) \tag{4.5}$$

Equation 4.6 shows the calculation of evaporative heat losses, $\dot{q}_{eva}$, following the reference [67].

$$\dot{q}_{eva}(x_s, t) = \frac{0.82\Delta H_v^*}{\sqrt{2\pi M R T_s}} P_0 \exp\left(\frac{\Delta H_v^*(T_s - T_v)}{R T_s T_v}\right) \tag{4.6}$$

The effective surface loss, $\dot{q}_{eff}$ is computed as the sum of convective, radiative, and evaporative surface losses as shown in Equation 4.7.

$$\dot{q}_{eff} = \dot{q}_{con} + \dot{q}_{rad} + \dot{q}_{eva} \tag{4.7}$$

4.2 Material Properties

Including the temperature-dependent material properties in the model is a crucial point to estimate the temperature distribution in the DED process and predict the formation and geometrical shape of the melt pool. The temperature-dependent material properties are integrated into the model separately for the IN718 used as feedstock powder material and for the SS316L used as the substrate material. More realistic results for melt pool geometry were got if the temperature-dependent properties instead of constant substrate properties.

The material properties of IN718 as feedstock material and SS316L as substrate material for solid and liquid phases are shown in Table 4.1 and Table 4.2, respectively. These values are the recommended material properties from [68]. The material comprises two different states: liquid and solid. ω has used an indicator to identify different material states.

- fluid (ω = 0)
- solid (ω = 1)

The rule of mixtures computes any property in the fluid-solid state transformation regime. Equation 4.8 shows the application of the rule of mixtures method to find the property at the corresponding state by using the solid volume fraction, f_s. Equation 4.8 shows an example calculation for the density of the matter, ρ, using the density of solid, ρ_s, and liquid, ρ_l, phases.

$$\rho = f_s \rho_s + (1 - f_s) \rho_l \quad (4.8)$$

Table 4.3 shows the solid volume fraction during heating and cooling of IN718 material.

Table 4-1 Thermophysical properties of IN718 material [68].

	Temperature (T)	**Mass Density** $(\rho_{s,l})$	**Specific Heat** $(C_{p\,s,l})$	**Conductivity** $(k_{s,l})$
Phase	$[K^0]$	$[kg/m^3]$	$[J/kg/K^0]$	$[W/m/K^0]$
Solid	298	8190	435	8,9
Solid	373	8160	455	10,8
Solid	473	8118	479	12,9
Solid	573	8079	497	15,2
Solid	673	8040	515	17,4
Solid	773	8001	527	18,7
Solid	873	7962	558	20,8
Solid	973	7925	568	21,9
Solid	1073	7884	680	26,9

Solid	1173	7845	640	25,8
Solid	1273	7806	620	26,7
Solid	1373	7767	640	28,3
Solid	1443	7727	650	29,3
Liquid	1609	7400	720	29,6
Liquid	1673	7340	720	29,6
Liquid	1773	7250	720	29,6
Liquid	1873	7160	720	29,6

Table 4-2 Thermophysical properties of SS316L material [68].

	Temperature (T)	**Mass Density** $(\rho_{s,l})$	**Specific Heat** $(C_{p\,s,l})$	**Conductivity** $(k_{s,l})$
Phase	$[K^0]$	$[kg/m^3]$	$[J/kg/K^0]$	$[W/m/K^0]$
Solid	300	7954	499	13,96
Solid	400	7910	512	15,53
Solid	500	7864	525	17,10
Solid	600	7818	538	18,68

Solid	700	7771	552	20,25
Solid	800	7723	565	21,82
Solid	900	7674	579	23,39
Solid	1000	7624	592	24,96
Solid	1100	7574	605	26,53
Solid	1200	7523	618	28,10
Solid	1300	7471	632	29,67
Solid	1400	7419	645	31,25
Solid	1500	7365	658	32,82
Solid	1600	7311	671	34,39
Solid	1700	7256	685	35,96
Liquid	1750	6979	770	17,98
Liquid	1800	6920	770	18,31
Liquid	1900	6857	770	18,64
Liquid	2000	6791	770	18,97
Liquid	2100	6721	770	19,30

Table 4-3 Solid volume fraction, fs, as a function of temperature [K] during melting of IN 718 [68].

Solid Volume Fraction (f_s)	**0**	**0.1**	**0.2**	**0.3**	**0.4**	**0.5**	**0.6**	**0.7**	**0.8**	**0.9**	**0.95**	**1**
Heating	1619	1614	1609	1604	1599	1592	1584	1575	1563	1552	1539	1523
Cooling	1608	1605	1601	1597.5	1593	1588	1583	1573	1564	1550	1536	-

Table 4.4 shows the emissivity values for IN718 material, according to the reference [69].

Table 4-4 Emissivity versus temperature for IN718 [69].

Temperature (T)	$[K^0]$	543	558	757	873	882	1016	1067	1119	1281	1369
Emissivity ($\in$)	$[W/m^2/K^0]$	0.23	0.24	0.26	0.28	0.28	0.3	0.31	0.31	0.32	0.33

4.3 Process Parameters in the Model

Process parameters are defined in the model to simulate the process as much as possible in the comparisons with the experiments. Two of them, laser power and scanning speed, were selected as the primary variable parameters to examine their effects on the temperature distribution and because of this on the melt pool geometry, and this situation was stated in Chapter 3, Experiments. Table 4.5 shows the process parameters used in the DED AM experiments and the developed thermal model for the DED process. Process parameters include laser power (P), scanning speed (v), return speed (v_r) used to calculate dwell time between layers, laser beam radius (r), layer thickness (d) free convective coefficient (h_{con}), forced convective coefficient (h_{for}) and ambient temperature (T_{amb}). The same parameters are used in single-track and multi-layer simulations, while the return speed is not used in single-track builds due to the waiting time between layers and the tool path not returning to the starting point of the layer. The efficiency factor or the absorption coefficient, η, which is mentioned with both names in the literature, significantly affects the resulting temperatures. The constant was chosen as 0.6 in this study.

Table 4-5 Process parameter sets for experiments and developed model.

Description	Process Parameter	Unit	Value
Laser Power	P	W	1500, 2000, 2500
Scan Speed	v	mm /s	12.5, 16.7, 22.2
Return Speed	v_r	mm /s	50
Laser Beam Radius	r	mm	1.5
Layer Thickness	d	mm	0.45
Free Convective Coefficient	h_{con}	W/ m^2 / K	15
Forced Convective Coefficient	h_{for}	W/ m^2 / K	35
Ambient Temperature	T_{amb}	K	298

4.4 Time Incrementation

To model the process accurately, time increment Δt must be created correctly and revealed in the model. Two constraints have been added to the developed model to reflect the time increment as precisely as possible. To prevent possible jumps between two consecutive locations, a time increment value smaller than the critical threshold value should be selected. Two of the defined process parameters are used to determine the time increment value in the model, as shown in Inequality 4.8. The first of these is the laser beam diameter (r_x) in the x-direction, which is the feed (scan) direction of the laser, and the scanning speed (v). With the increase in scanning speed, time increments consisting of smaller time intervals were created.

$$\Delta t < \frac{r_x}{v} \tag{4.8}$$

Time increment, Δt, secure the movement of the heat source within its effective region Along with the similar work in [70], a factor, f_{op}, is used here to ensure the overlap of successive regions affected by consecutive heat, as shown in Equation 4.9. Time stepping generates automatically during analysis according to a specific temperature rise setting in the simulations. To achieve the desired precision of the results, an upper limit ΔT of 50 K has been defined for the temperature increase between two consecutive time increments. ($0 \leq f_{op} \leq 1$).

$$\Delta t = f_{op} \frac{r}{v} \tag{4.9}$$

4.5 Finite Element Model

The FE model constructed for the temperature field is obtained by discretizing the temperature field and using the weak form of the transient energy balance shown in Equation 4.1. Figures 6,7, and 8 show the mesh and boundary conditions used in single-track simulations consisting of 14,520 elements and 18,166 nodes for 12.5 mm / s scanning speed conditions, one of the sample model analyses sets. The number of elements generated in analyzes depends on the scanning speed. As a result, the number of elements and nodes in the generated mesh is in various cases and between analyzes. As shown in Figure 6, different material properties are assigned to the substrate and the build layer. The initial temperature of the substrate temperature was determined as 323 K, which is also used as the initial condition for all elements in the network and is shown in Figure 7. As seen in Figure 8, moving volumetric heat flux and fixed substrate temperature of 323 K at the bottom surface are defined as thermal boundary conditions.

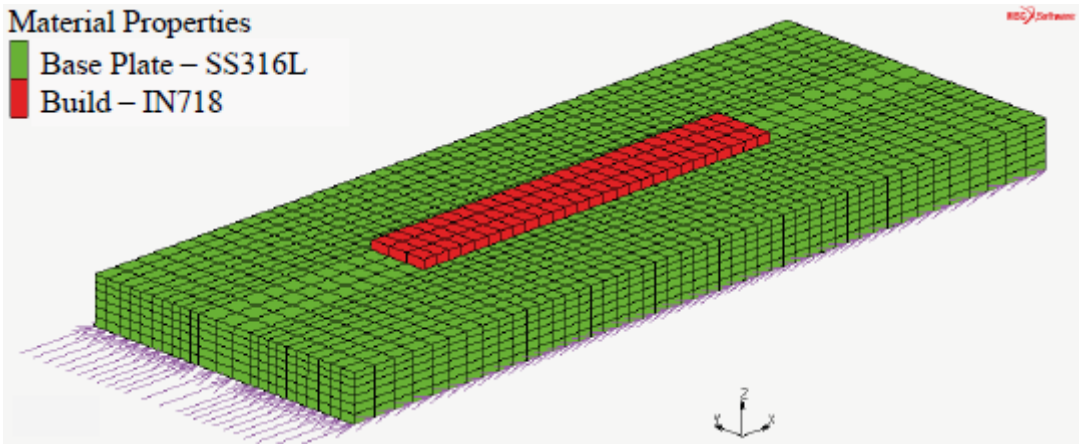

Figure 4-1 Defined material types.

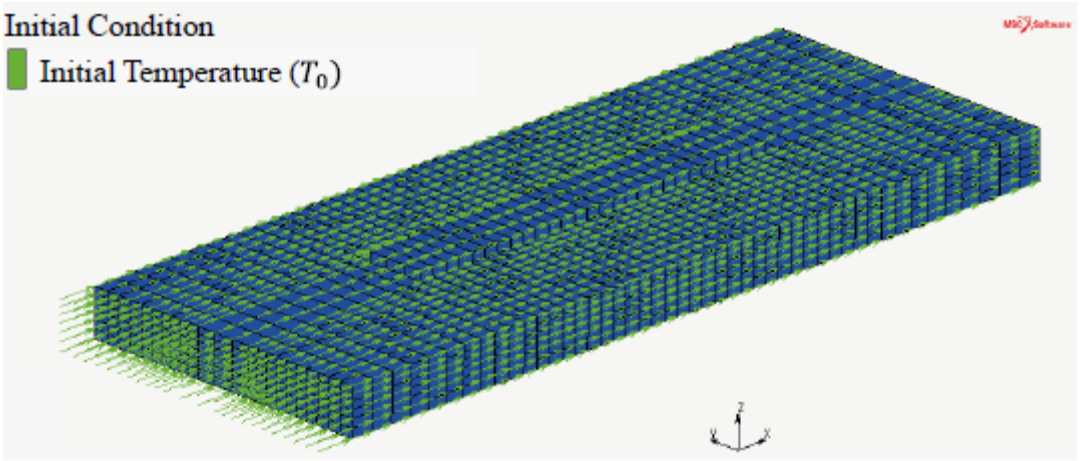

Figure 4-2 Defined initial conditions.

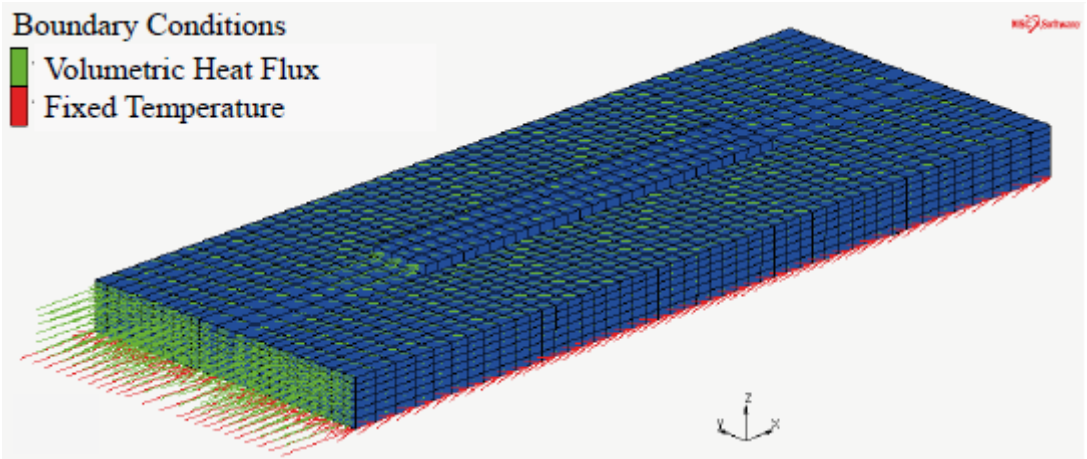

Figure 4-3 Defined boundary conditions.

Equation 4.10 shows the definition of the element size. To determine the element size in the analyzes in the model, the time increment limit was used, as shown in Inequality 4.8. At the size to be obtained by adjusting the element size in this way, it will be such that the motion of the heat source remains inside the element during a time step. To meet this criterion, an additional mesh refinement factor, f_{ref}, was defined during model creation ($0 \leq f_{ref} \leq 1$).

$$\Delta x = \frac{r_x}{f_{ref} f_{op}} \tag{4.10}$$

The finite element model study was performed using MSC MARC® commercial software. In addition to that, several user-defined subroutines were used simultaneously for different purposes [71]. These user-defined subroutines and their aims are listed in Table 4.6.

In this study, a novel approach is followed to define the surface heat losses shown previously in Equation 4.7. Surface boundary conditions were expressed in negative volumetric heat sources for the topmost elements for the newly added layer. Therefore, this eliminated another subroutine (FILM) to define the surface heat losses and identification of those surfaces after each layer addition. The surface heat loss integral was converted to a volumetric integral using the divergence theorem to achieve that. Therefore, for the heat loss from a single surface, the amount of surface heat loss can be expressed with Equation 4.11, in which $\dot{q}_{eff}$ and
d are the overall effective surface loss and layer thickness, respectively. The surface losses from the topmost surfaces of a newly added layer neglecting the losses from the side surfaces are assumed only. This equation is applicable for one element per layer.

$$\dot{Q}_{eff} = \frac{\dot{q}_{eff}}{d} \tag{4.11}$$

Figure 4.4 shows the flowchart of the developed model with used several software and to generate required inputs and how to use them between software environments to analyze the developed thermal model.

Subroutine	Description
FLUX	For heat transfer analysis, it allows user to specify surface or body fluxes as a function of the time, position, or temperature. It defines the moving heat flux.
UBINC	At the beginning of each increment, state variable updates.
UACTIVE	It can be used to either activate or deactivate elements in the model based on a criterion. Can be called at the beginning of the analysis and at the end of each increment.
ANKOND	For anisotropic heat transfer analysis, it can be chosen by user to define an anisotropic conductivity matrix at each integration point for every element at liquid or solid states.
USPCHT	To define the specific heat or heat capacitance, it is called at each increment for every element in the mesh.
INTCRDS	To find the integration point coordinates once at the initialization.
UTIMESTEP	To set the minimum time increment during deposition and inter-layer time.

Table 4-6 Definition of subroutines used in model [71].

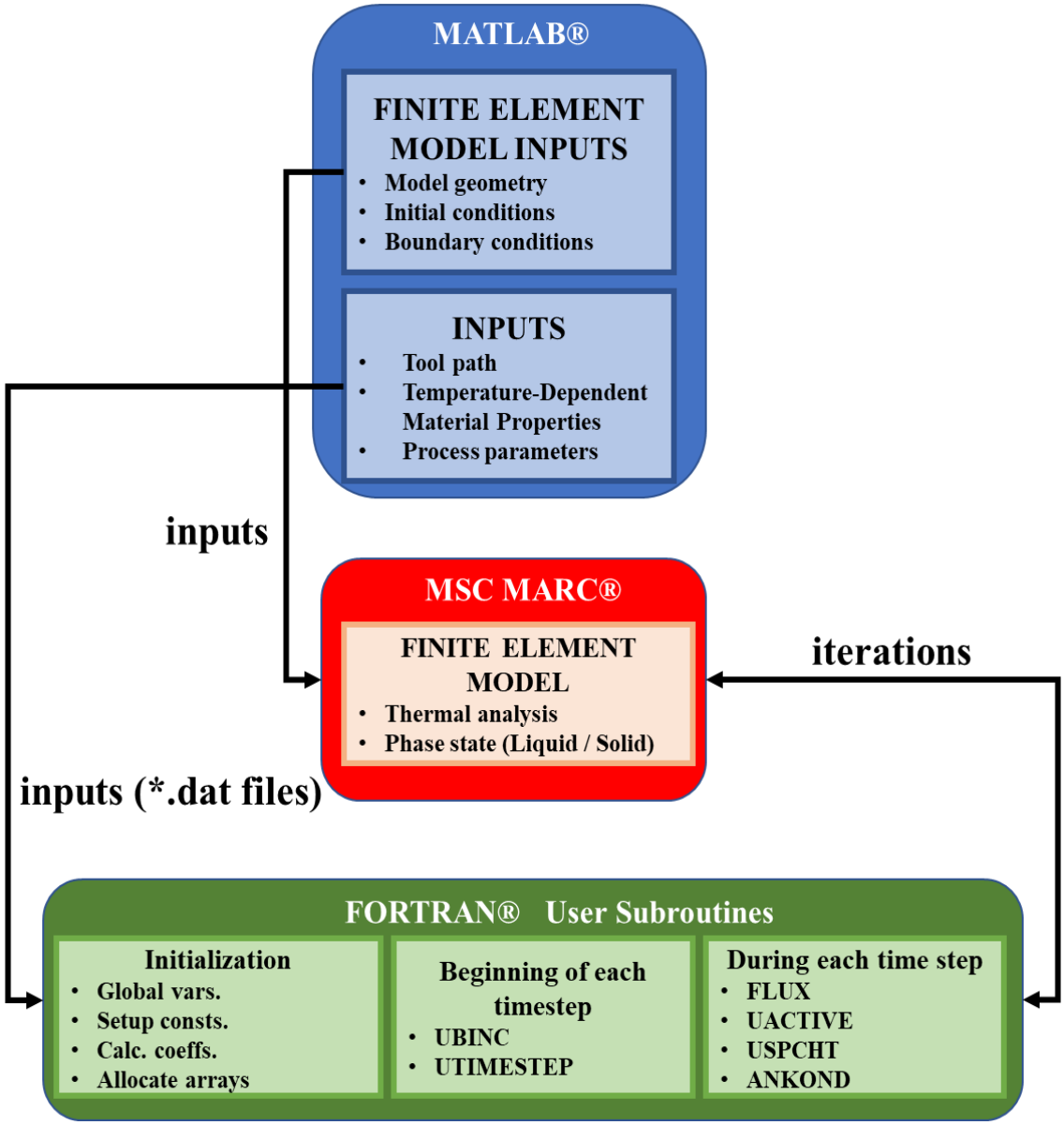

Figure 4-4 Flowchart of different software environments used for the generation of the inputs (MATLAB®), finite element analysis(MSC MARC®), together with user defined subroutines (Fortran®).

5. RESULTS and DISCUSSION

5.1 Single-Track Melt Pool Depth and Width Comparisons

Figure 5.1 is an example from the experimental set showing the alignment method and visual explanation of the measurements for melt pool depth and width images taken from the ex-situ microscope measurements and the model. The melt-pool boundaries in the simulations were identified by the temperature contours of liquidus temperature of 1833 K. Experimental boundaries were measured from the baseplate (z=0) level from the OM results. For microscope images, depth and width values were calculated by measuring the length of the two points between the boundary points of the deposited material and the substrate material. In the model, the value of 1833 K, which is the referenced temperature value of melt pool temperature during experiments by AM machine software, was accepted as the limit and measurements were made accordingly. The scale bar is set the same for all plots from model.

Nine images in Figure 5.2 through Figure 5.10 show the images analyzed from cross sections of nine parts with different laser power and scan speed values as a result of ex-situ work in single-track depositions. The results obtained show the effect of laser power and scanning speed, which are defined as variables in the experiments performed and whose effect is aimed to be observed, on the melt pool cross-sections. A qualitative investigation of the resulting maps reveals several important observations. It was observed that the width of the melt pool formed because of the interaction of the laser and the fed powder increased with the increasing laser power, while the increase in laser power also caused a spread in the track profile. The effect of laser parameters on the shape and size of the laser melt pool can also be demonstrated and characterized using the energy density formula. Penetration depth was noticeably lower at lowest Linear Energy Density (LED) value with (1500 W) and high velocity (22.2 mm / s) compared to experiments where other process parameter sets were applied. Eqn. 5.1, 5.2 and 5.3 describe LED, Areal Energy Density (AED) and Volumetric Energy Density (VED) formulations respectively in terms of laser power, scan speed, laser spot size and hatch (track) distance of laser feed. The laser spot size is constant throughout the study. The tool path created for the hatch distance must be offset in the y-direction and the new deposit must proceed on this path. However, since both single-track and multi-layer deposits currently travel on a single path, this parameter is not available in experiments and models either.

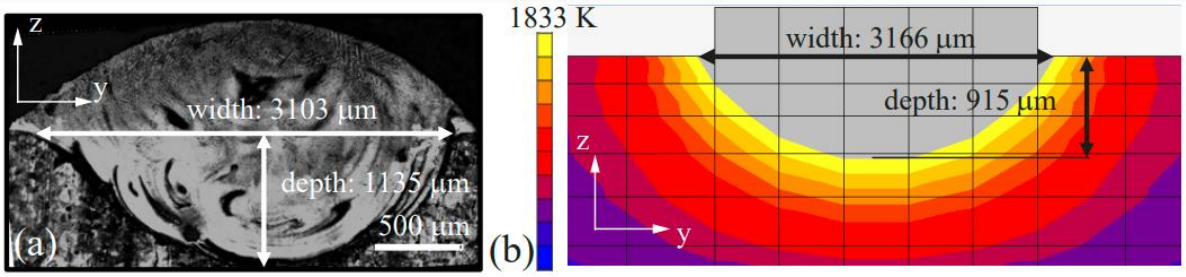

Figure 5-1 Example image to show melt-pool size (depth and width) measurements for single-tracks: a. Experimental images from OM analysis. b. Temperatures from the finite element simulations.

$$\text{LED}\ \left[\frac{Joule}{mm}\right] = \frac{\text{Laser Power}\ [W]}{\text{Scan Speed}\ [\frac{mm}{s}]} \tag{5.1}$$

$$\text{AED}\ \left[\frac{Joule}{mm^2}\right] = \frac{\text{Laser Power}\ [W]}{\text{Scan Speed}\ \left[\frac{mm}{s}\right]\ x\ \text{Laser Spot Size}\ [mm]} \tag{5.2}$$

$$\text{VED}\ \left[\frac{Joule}{mm^3}\right] = \frac{\text{Laser Power}\ [W]}{\text{Scan Speed}\ \left[\frac{mm}{s}\right]\ x\ \text{Laser Spot Size}\ [mm]\ x\ \text{Hatch (Track) Distance}\ [mm]} \tag{5.3}$$

While the scanning speed was kept the same (22.2 mm / s), the gradually increasing power between 1500 and 2500 W caused the penetration depth to increase at this scanning speed. This observed situation does not seem to be noticeably significant at this level in the remaining two scan speed levels. Based on this effect observed in the experiments, 22.2 mm / s, the highest scanning speed selected in the test set, can be accepted as a critical maximum limiting value to ensure proper fusion of the building layers to the underlying layer and the sustainability of a solid structure formation.

When the cross-sectional areas of the samples were examined, the penetration of the deposited single-track into the substrate was not aligned symmetrically with the axis of the melt pool, which is related to the inhomogeneity of the material geometry being deposited. Although the source of this observed off set is not clearly known, but it is believed to happen during the melt state of the deposit within the interaction of substrate's top surface. It was believed that Argon gas and associated cooling effects during the process caused an inhomogeneous geometry of the deposit geometry.

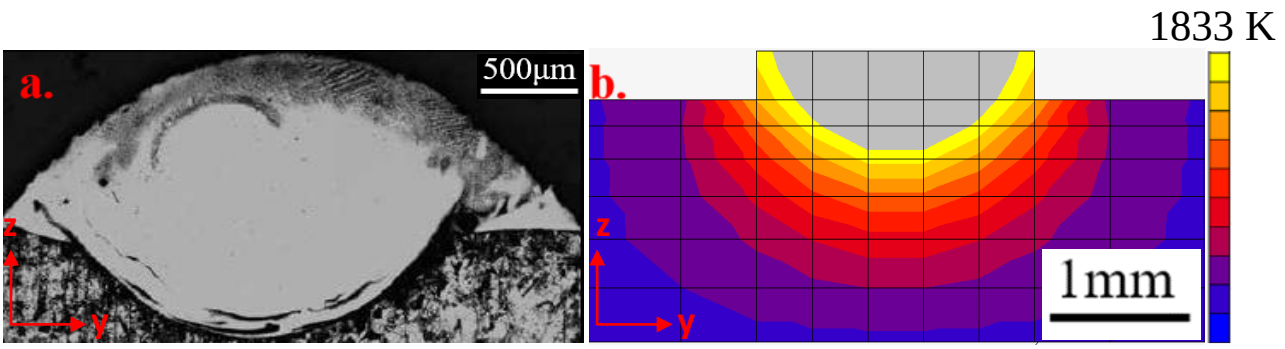

Figure 5-2 Melt-pool depth and width comparison. a. Experimental images from OM analysis. b. Temperatures from the finite element simulations. Process parameters: 1500 W and 12.5 mm/s for laser power and scan speed, respectively.

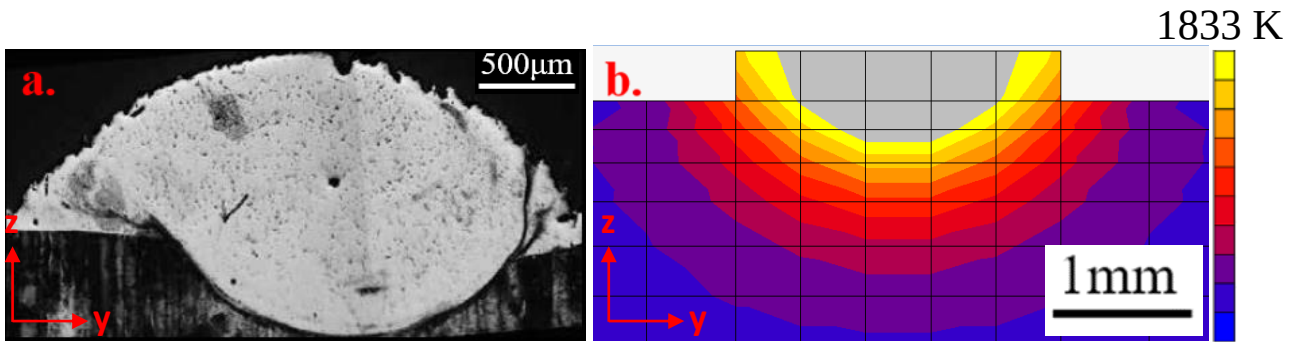

Figure 5-3 Melt-pool depth and width comparison. a. Experimental images from OM analysis. b. Temperatures from the finite element simulations. Process parameters: 1500 W and 16.7 mm/s for laser power and scan speed, respectively.

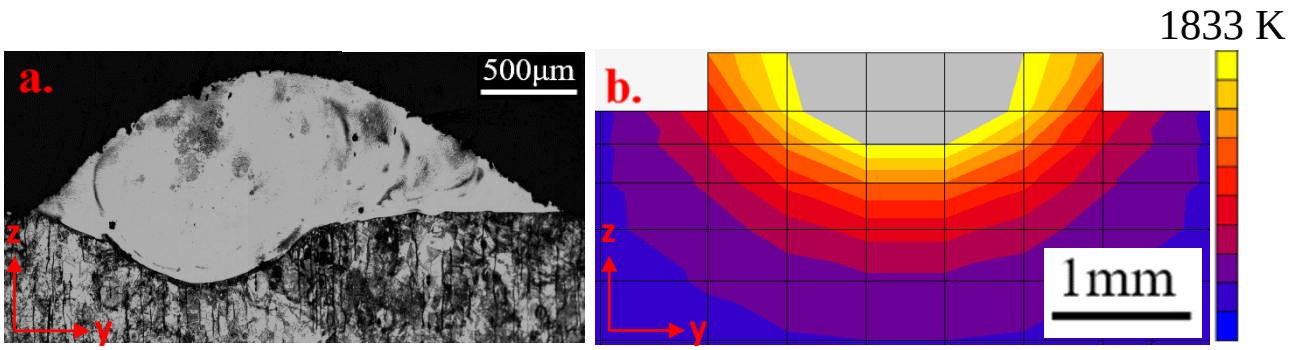

Figure 5-4 Melt-pool depth and width comparison. a. Experimental images from OM analysis. b. Temperatures from the finite element simulations. Process parameters: 1500 W and 22.2 mm/s for laser power and scan speed, respectively.

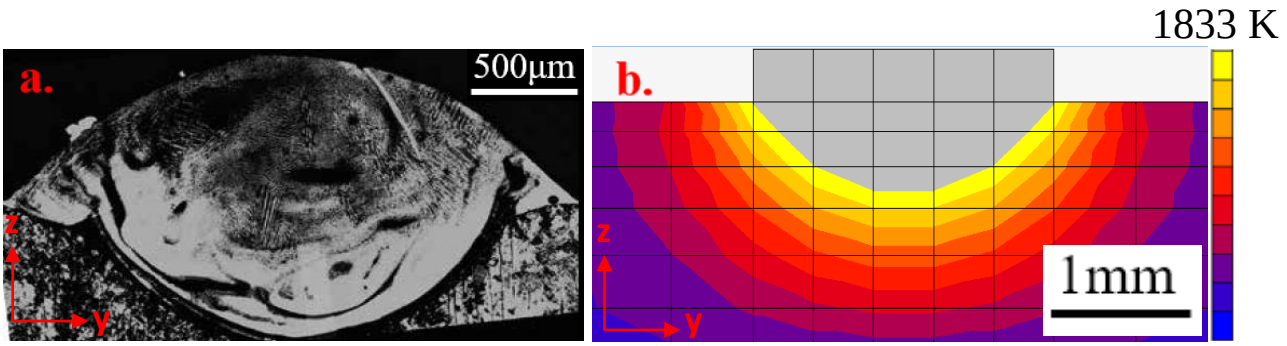

Figure 5-5 Melt-pool depth and width comparison. a. Experimental images from OM analysis. b. Temperatures from the finite element simulations. Process parameters: 2000 W and 12.5 mm/s for laser power and scan speed, respectively.

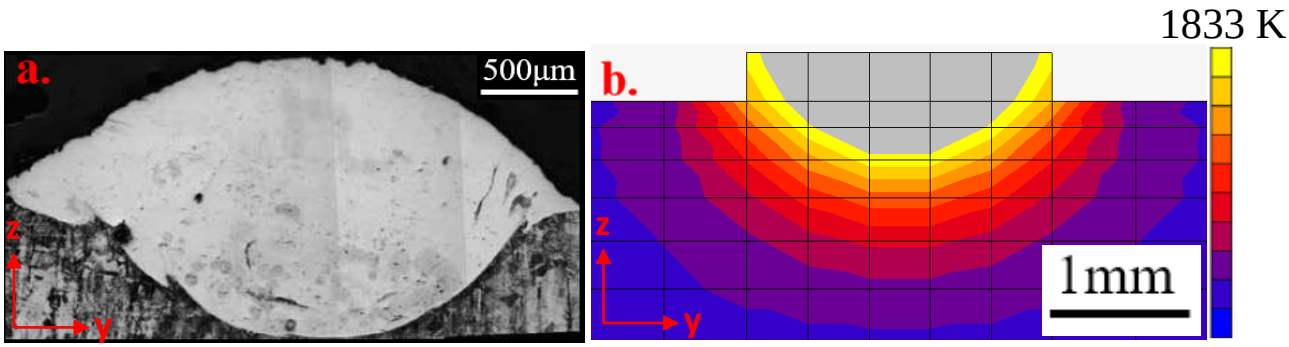

Figure 5-6 Melt-pool depth and width comparison. a. Experimental images from OM analysis. b. Temperatures from the finite element simulations. Process parameters: 2000 W and 16.7 mm/s for laser power and scan speed, respectively.

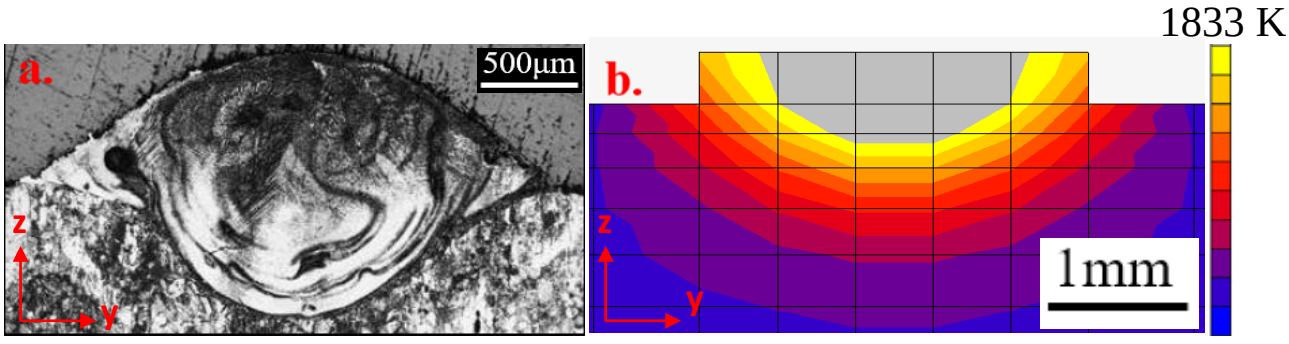

Figure 5-7 Melt-pool depth and width comparison. a. Experimental images from OM analysis. b. Temperatures from the finite element simulations. Process parameters: 2000 W and 22.2 mm/s for laser power and scan speed, respectively.

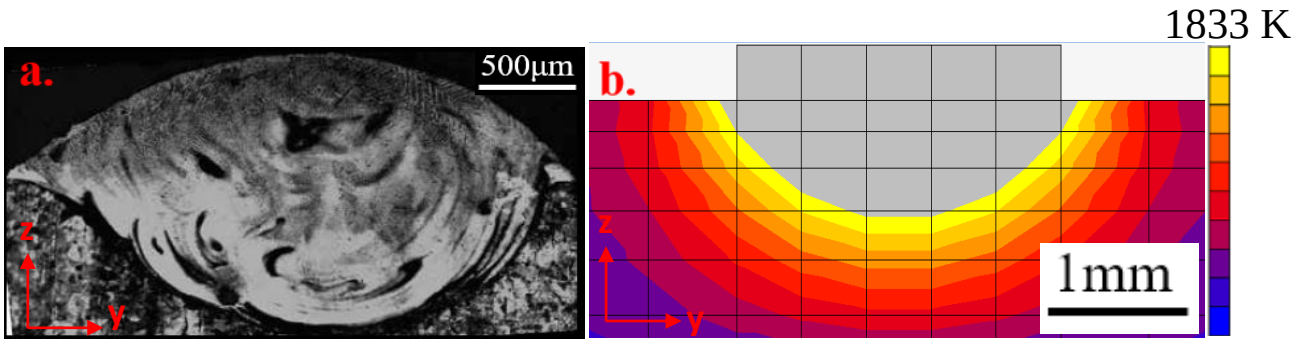

Figure 5-8 Melt-pool depth and width comparison. a. Experimental images from OM analysis. b. Temperatures from the finite element simulations. Process parameters: 2500 W and 12.5 mm/s for laser power and scan speed, respectively.

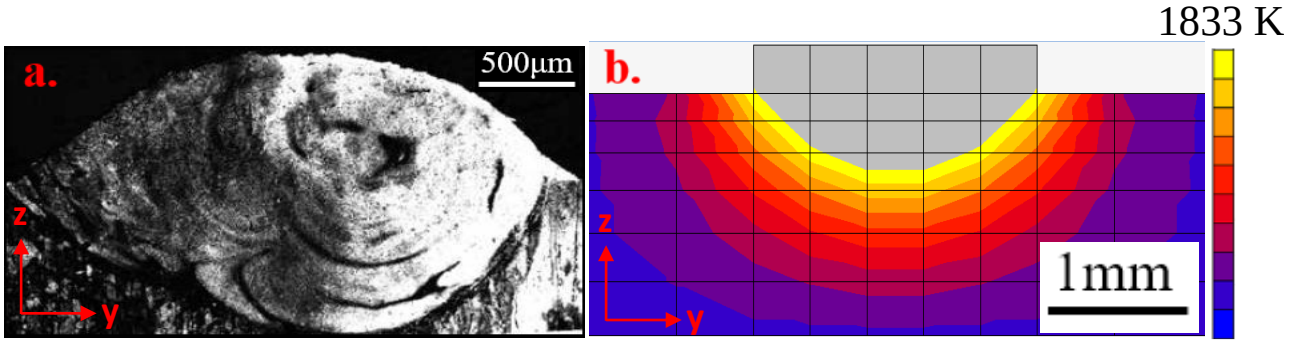

Figure 5-9 Melt-pool depth and width comparison. a. Experimental images from OM analysis. b. Temperatures from the finite element simulations. Process parameters: 2500 W and 16.7 mm/s for laser power and scan speed, respectively.

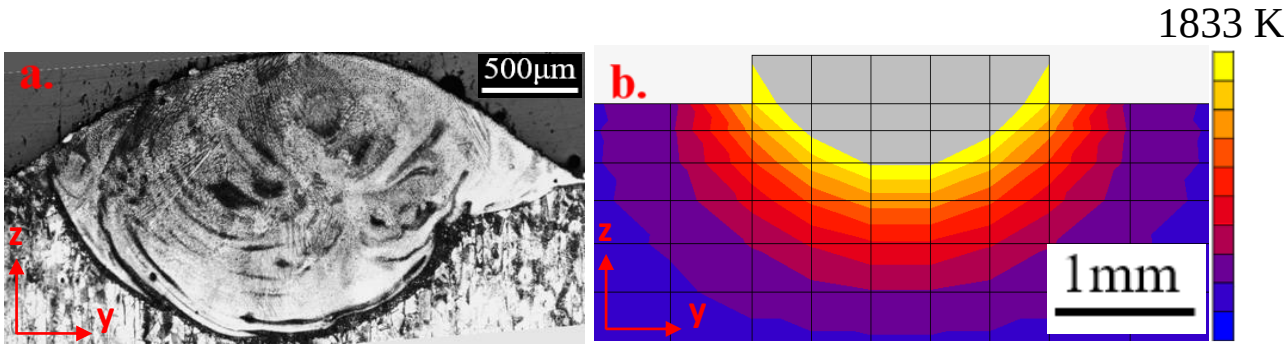

Figure 5-10 Melt-pool depth and width comparison. a. Experimental images from OM analysis. b. Temperatures from the finite element simulations. Process parameters: 2500 W and 16.7 mm/s for laser power and scan speed, respectively.

Figures 5.2 to 5.10 show OM results of melt pool sections for IN718 alloy processed by the DED method to SS316L substrate. In the experiments, it was observed that when the scanning speed increased, there was a decrease in the height of the melt pool from 12.5 mm / s to 22.2 mm / s. The similar results were observed in the study of Bax *et al*. [72], conducting their experiments with the identical AM machine equipment of this thesis study and IN718 powder-fed material for deposition, and reported in their study that the scanning speed increased and height are in reciprocal proportion relationship. With this knowledge, it has been observed that an increase in scanning speed can almost always be associated with a decrease in melt pool height for any laser power parameter (1500 W, 2000 W and 2500 W) used in the present study. In a previously reported study [73], it was shown that increasing laser power from 1000 W to 2000 W did not cause a significant increase in melt pool height. However, in another study conducted at different laser power ranges, it was reported that when the IN718 was processed with the DED method; it was observed that the melt pool height increased as the laser power increased from 400 W to 1000 W [74]. Based on the results of the current study and the findings of previous literature studies, it is accurate to say that; it is possible to conclude that the increase in scanning speed is not always associated correlation with an increase, decrease or no change at all. Studies with different laser power values show that the different laser power ranges used for comparison are important and may give different tendencies.

It is a known fact from many previous studies that the melt pool morphology of a material is sensitive to processing parameters [75], [76]. When looking at the values of melt pool width and depth, it is observed that these values tend to increase with increasing laser power from 1500 W to 2000 W and from 2000 W to 2500 W for almost all conditions. This situation reveals an opposite finding to that observed when the scanning speed is increased. Similar conclusion has been conducted in other studies that increase in laser power values effects cross-sectional area of the deposited single track geometries, which becomes larger [72] and the melt pool size increases with increasing laser power and decreasing and scanning speed as a conclusion of the referenced study. All melt pool images from single-track depositions in the present study reveal the presence of dilution consistent with those observed by Wolff *et al.* [73]. As indicated in the referenced study, dilution is present when the laser power is above 1000 W. The dilution of the melt pool to the substrate material or between preceding and current layer is used for characterization of the melt pool geometry. A previous reported work [77] done by Toyserkani defines the dilution, D as the ratio of penetration depth, h, to the

overall size of the melt zone that is the sum of the penetration depth and layer thickness, d as in Equation 5.4 to quantify the bond between the melted, deposited material and the substrate.

$$D = \frac{h}{h+d} \tag{5.4}$$

The amount of dilution depends on the thermal history and melt pool properties such as cooling rate [78]. Both dilution and another melt-pool characteristic, the melt-pool depth, have a non-linear relation with processing parameters [76]. When the deposition material and the substrate material are different, for example, when the γ-TiAl alloy is deposited on the titanium alloy substrate, low dilution values (about 0.06) were targeted, and thus great microhardness values were obtained [76]. If the nickel-based alloy as used in this study is selected as the deposition material, it is aimed to obtain a dilution value of less than 0.6, because values higher than this result in excessive melting of the substrate material that is not suitable for passing the standards and the desired condition cannot be achieved from the part [79]. A similar study result, Wolff et al., by building layers of IN718 material laser deposition on a carbon steel substrate, they achieved a dilution of around 0.5 [73].

The dilution values in this thesis study are calculated and given as a function of increasing laser power from 1500 W to 2500 W as; **0.39**, **0.47** and **0.46**, respectively, for the scan speed of 12.5 mm/s; **0.37**, **0.48** and **0.46**, respectively, for the scan speed of 16.7 mm/s; and **0.33**, **0.52** and **0.46**, respectively, for the scan speed of 22.2 mm/s. The dilution pertained to 12.5 mm/s and 16.7 mm/s processed samples are observed to increase with increasing laser power up to 2000 W, and then saturates, whereas the value of 22.2 mm/s does not exhibit any tendency. The obtained values in the current study are comparable to the dilution what was obtained by Wolff *et al*. [73]. In this study, an increase in the clad height below the substrate as a function of increasing laser power is a witnessed phenomenon. Similarly, Petrat *et al*. demonstrated the clad height increase with increasing processing power [74]. A similar behavior is observed in the current work, where the greatest d values are obtained at 2500 W laser power processed samples.

Tables 5.1 and 5-2 show general results, comparisons, and error values of melt pool sizes for experimental measurements and simulation findings for width and depth, respectively. The simulation results usually overestimate the resulting widths of the melt pools to a maximum of 24% error. For the depth values and the comparison, it is revealed that the simulation study

calculates the depths of the melt pool with a maximum error of 36% and almost always underestimates it.

Table 5-1 Melt-pool width for single-track deposition. Comparison experimental OM measurements versus simulation results.

		Melt Pool Width		
Laser Power [W]	**Scan Speed [mm/s]**	**Experiment [µm]**	**Simulation [µm]**	**Error [%]**
1500	12,5	1755	2176	24
1500	16,7	1632	1812	11
1500	22,2	1500	1506	1
2000	12,5	2397	2870	20
2000	16,7	2154	2232	4
2000	22,2	1785	1675	-6
2500	12,5	3103	3166	2
2500	16,7	3055	2725	-11
2500	22,2	2264	2418	7

Table 5-2 Melt-pool depth for single-track deposition. Comparison experimental OM measurements versus simulation results.

		Melt Pool Depth		
Laser Power [W]	**Scan Speed [mm/s]**	**Experiment [µm]**	**Simulation [µm]**	**Error [%]**
1500	12,5	524	478	-9
1500	16,7	426	372	-13
1500	22,2	305	264	-13
2000	12,5	720	735	2
2000	16,7	599	492	-18
2000	22,2	543	345	-36
2500	12,5	1135	915	-19
2500	16,7	738	665	-10
2500	22,2	681	575	-16

The proposed numerical model for estimating melt pool characteristics fits well with the experimental results of the present study, as shown in Tables 5.1 and 5.2. In the developed model, the melt pool width and depth appear to be predictable with approximately 24% and 36% accuracy, respectively, in the worst cases. A higher level of accuracy was generally obtained for simulations corresponding to experiments with the remaining process parameters except for these two worst cases. Comparison of this value with the previously reported literature reveals the predictive capacity of the current method. For example, the depth value in the DED process for IN718 material was previously calculated with 75% accuracy [72]; this appears to be almost identical to those obtained in the current study to estimate the melt pool depth. The melt pool width and depth of the metal PBF process, which has high similarities with the DED process to model, were experimentally found to be 158µm and 76µm, respectively, by Promoppatum et al. [79]. It is estimated by the developed method that these are around 204µm and 62µm, respectively. This result obtained shows an estimation rate accuracy of 71% and 82%, respectively, for melt pool width and depth. Hernando et al. with the model developed for laser beam welding, a process like DED, it estimated the welded melt pool width and depth of the IN718 with 90% and 96% accuracy, respectively [80]. The good correlation seen between numerical and experimental data in the present thesis study is an

indication that the proposed model can be useful for capturing the general interaction of laser and raw metal powder material.

5.2 Single-Track Melt Pool Area Size Comparisons

Left hand side portions (a.) of all images for Figure 5-11 to 5-19 show in-situ thermal camera images taken at approximately the center position of single-line structures where accumulation is expected to reach steady-state behavior. Generation of these necessary data in the machine during manufacturing, frame collection during each deposition, and raw data collection after manufacturing and how they are brought to this image output format showing the temperature distribution seen in the figures are explained with the image processing method explained in detail in Section 3.4. The scale bar is set the same for all plots.

As it is seen in the Figure 5-11 to 5-19, as the laser power increases, the maximum temperature increases correspondingly, increasing the HAZ and size of the melt zone. Reducing the scanning speed caused the LED to increase, the increased energy increased the transverse dimension of the melt zone (along the y-direction) and resulted in a round shape for the melt region rather than an elliptical shape. The generated figures clearly reveal that the laser power has a much more significant effect on the geometry of the melting zones and on the values of the highest temperatures compared to the scanning speed. As the laser power increases and the scanning speed decreases, that is, the smaller the area affected by the generated localized heat input and the higher the LED, the larger the area of the highest temperature.

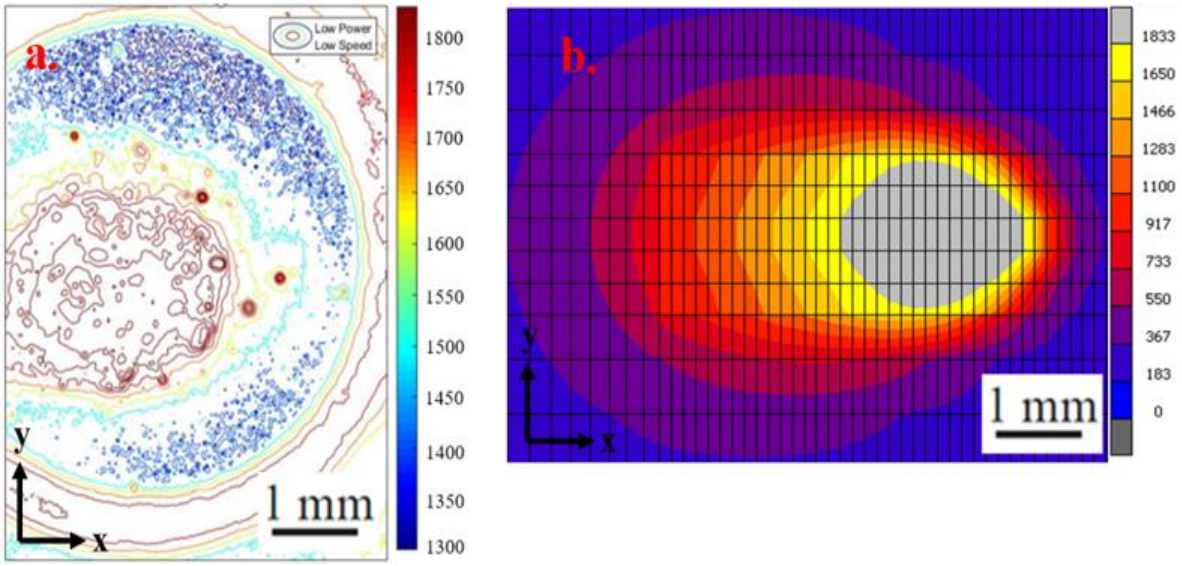

Figure 5-11 Melt-pool area size estimation. a. Experimental temperatures from in-situ IR camera measurements. b. Temperatures from the finite element simulations. Process parameters: 1500 W and 12.5 mm/s for laser power and scan speed, respectively.

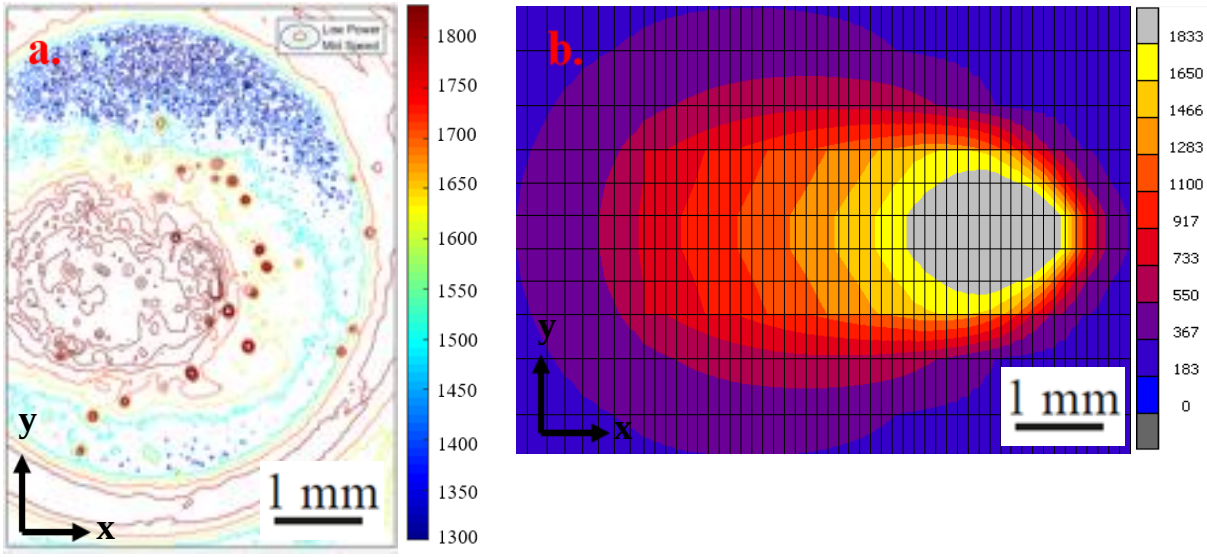

Figure 5-12 Melt-pool area size estimation. a. Experimental temperatures from in-situ IR camera measurements. b. Temperatures from the finite element simulations. Process parameters: 1500 W and 16.7 mm/s for laser power and scan speed, respectively.

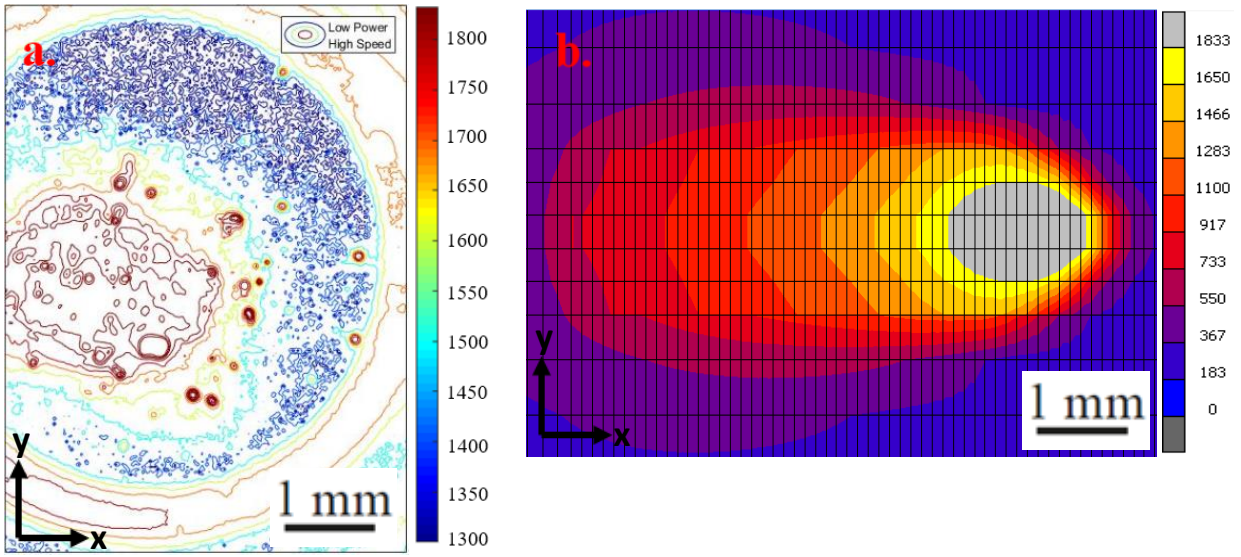

Figure 5-13 Melt-pool area size estimation. a. Experimental temperatures from in-situ IR camera measurements. b. Temperatures from the finite element simulations. Process parameters: 1500 W and 22.2 mm/s for laser power and scan speed, respectively.

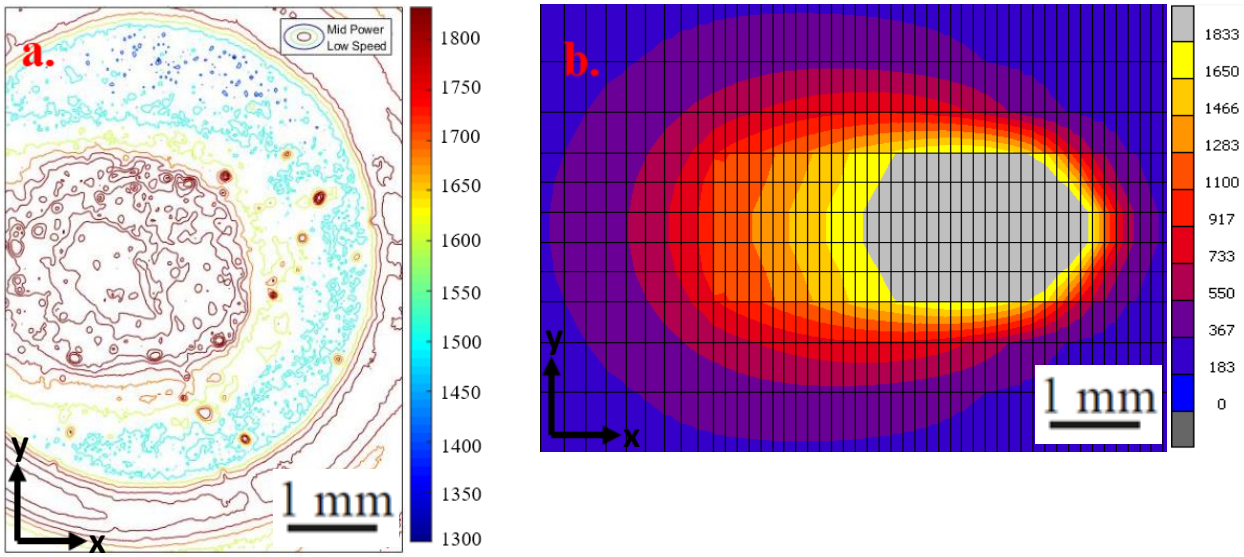

Figure 5-14 Melt-pool area size estimation. a. Experimental temperatures from in-situ IR camera measurements. b. Temperatures from the finite element simulations. Process parameters: 2000 W and 12.5 mm/s for laser power and scan speed, respectively.

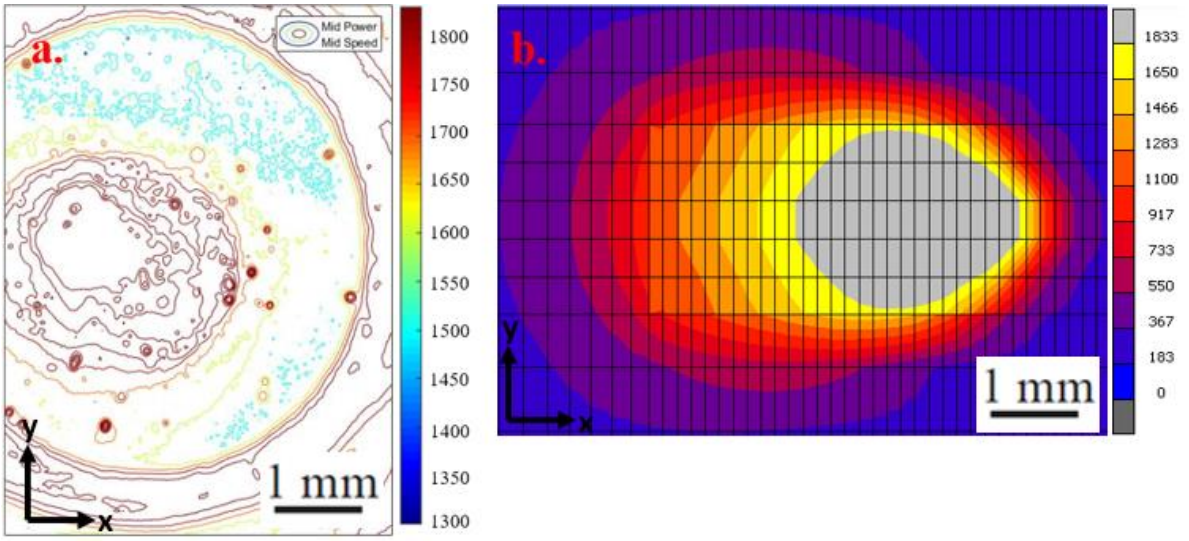

Figure 5-15 Melt-pool area estimation. a. Experimental temperatures from in-situ IR camera measurements. b. Temperatures from the finite element simulations. Process parameters: 2000 W and 16.7 mm/s for laser power and scan speed, respectively.

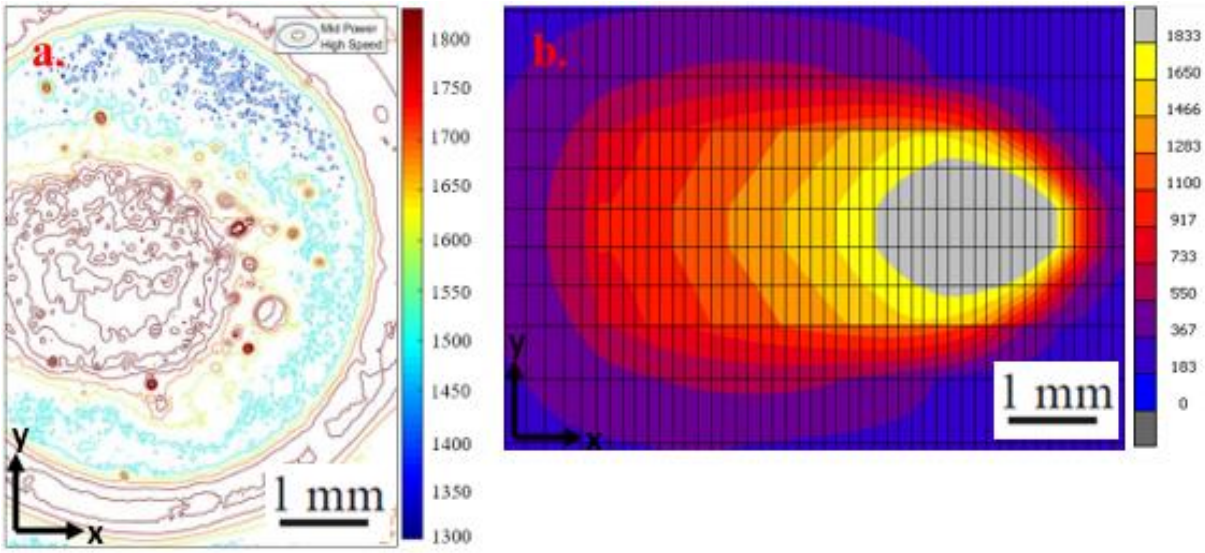

Figure 5-16 Melt-pool area size estimation. a. Experimental temperatures from in-situ IR camera measurements. b. Temperatures from the finite element simulations. Process parameters: 2000 W and 22.2 mm/s for laser power and scan speed, respectively.

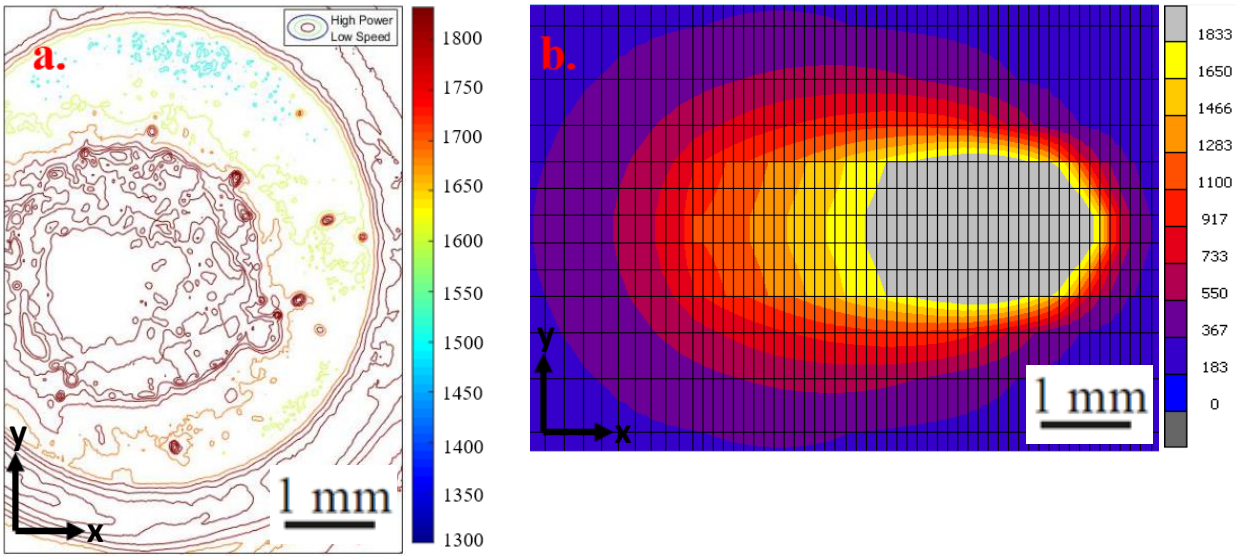

Figure 5-17 Melt-pool area size estimation. a. Experimental temperatures from in-situ IR camera measurements. b. Temperatures from the finite element simulations. Process parameters: 2500 W and 12.5 mm/s for laser power and scan speed, respectively.

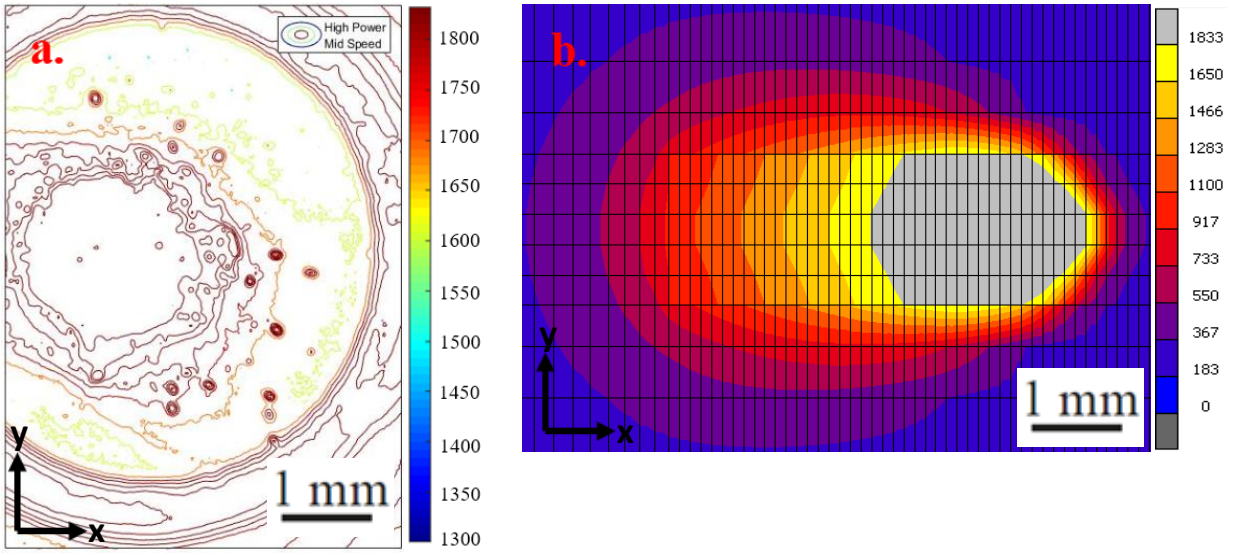

Figure 5-18 Melt-pool area size estimation. a. Experimental temperatures from in-situ IR camera measurements. b. Temperatures from the finite element simulations. Process parameters: 2500 W and 16.7 mm/s for laser power and scan speed, respectively.

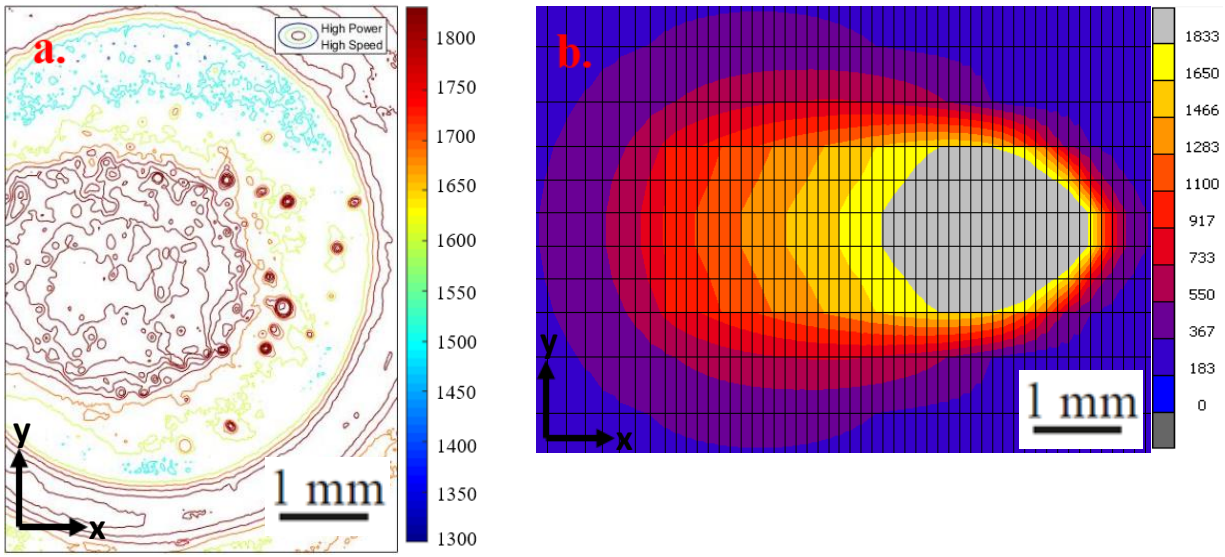

Figure 5-19 Melt-pool area size estimation. a. Experimental temperatures from in-situ IR camera measurements. b. Temperatures from the finite element simulations. Process parameters: 2500 W and 22.2 mm/s for laser power and scan speed, respectively.

Image processing with experimental in situ temperature measurement data correlated well with the simulation results when the liquidus temperature 1833 K melt pool as core temperature was used to define the melt zone. This result suggests almost 99.9% accuracy for determining the temperature of the melt pool. The temperature of the melt pool gradually changed from almost 1650 C to less than 400 C, over a distance of a few millimeters.

Table 5.3 shows the area of the melt pool regions experimentally measured and simulated for different process parameters in single-track deposits and compares these values. Results obtained by simulation often underestimated the amount of area of melt pools in all cases. This suggests using a higher efficiency factor, η, in simulations. The maximum deviation of the experimental melt pool area was 17% with lowest laser power and highest scan speed case, where the lowest penetration was also observed in OM ex-situ image analysis performed by investigating the cross sections, Figure 5-4.

Table 5-3 Comparison of experimental measurements obtained from thermal camera images and thermal simulation results for single-track builds.

		Melt Pool Area		
Laser Power [W]	**Scan Speed [mm/s]**	**Experiment [mm^2]**	**Simulation [mm^2]**	**Error [%]**
1500	12.5	6.88	6.48	-6
1500	16.7	6.28	5.36	-15
1500	22.2	5.04	4.2	-17
2000	12.5	9.46	8.8	-7
2000	16.7	8.19	7.1	-13
2000	22.2	5.24	4.94	-6
2500	12.5	12.7	11.2	-12
2500	16.7	10.5	10.12	-4
2500	22.2	8.74	8.79	1

5.3 Multi-Layer Micrograph Analysis

To understand the effect of laser power and scan speed process parameters on the fusion between deposited layers, multi-layer thin wall builds have been investigated by experiments. The fusion between the layers deposited with the same material type (IN718) contains relatively more important findings than the fusion created with the substrate material (SS316L). The reason for this is that after the AM is completed, the built part will be separated from substrate using various post processing equipment such as bandsaw, wire cut Electrical Dischange Machining (EDM) and waterjet cutting. For this reason, the cross-sectional areas of thin wall structures consisting of eight layers in total were prepared and examined, as shown in Figure 5-20.

As seen in Figure 5-20 (b), it was observed that the ideal multi-layer thin wall deposition geometry with almost vertical side walls was formed for process parameters of 1500 W - 16.7 mm/s. In addition, as the laser power increased to 2500 W, the melting of approximately all the formerly deposited layers occurs. Increased heat input caused by the increase in laser

power value and unwanted occurrence of overheating (excessive remelting of previous layers) phenomenon with the increase in LED value causes the layers to fuse deeper into the substrate, thus significantly reducing the height of the walls in a design-intent way, which results in using too high laser power proves it can cause dimensional inaccuracies. It is observed that scanning speed has a relatively lower effect on geometric tolerances than laser power. However, scanning speed can also affect the regularity of the melt zone. The scanning speed should be chosen slow enough to have a regular melting zone to be obtained, and fast should be selected at values that do not cause overheating, as Figure 5-20 (b).

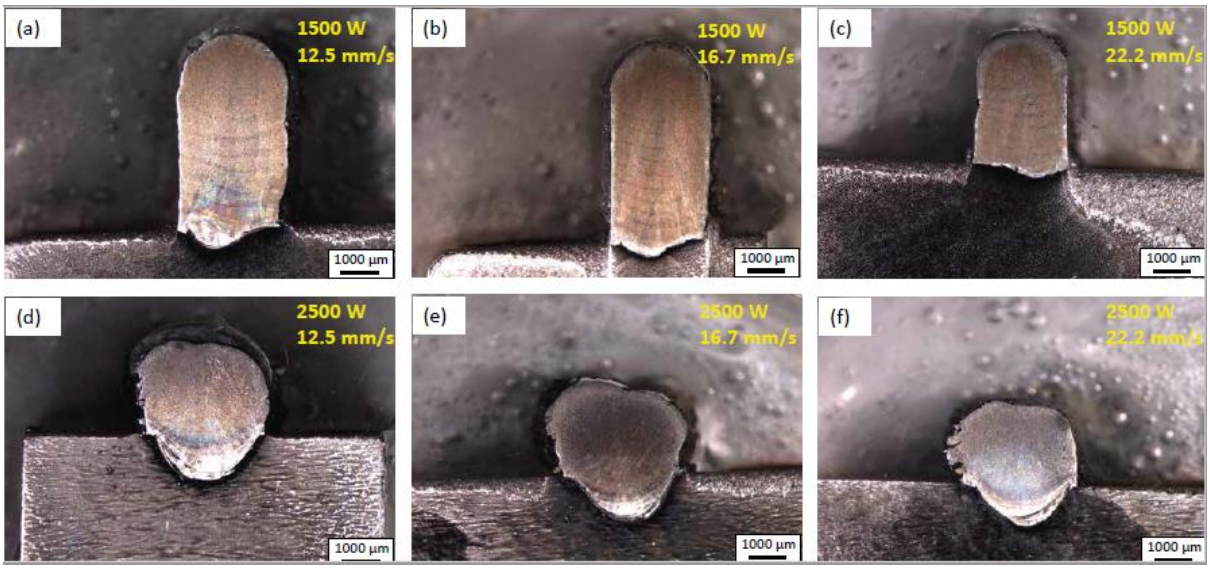

Figure 5-20 Multi-layer micrographs for: a. 12.5 mm/s - 1500 W, b. 16.7 mm/s - 1500 W, c. 22.2 mm/s - 1500 W, d. 12.5 mm/s - 2500 W, e. 16.7 mm/s - 2500 W and f. 22.2 mm/s – 2500 W.

5.4 Multi-Layer Melt Pool Area Size Comparisons

After the multi-layer deposition experiments, author determined the extreme cases for modeling and conclude analysis on these. By evaluating the findings revealed in the microscope images, it was compared the experiments with the lowest power, lowest speed, highest speed, and highest power cases within the analysis. As a result, three experiments with these selected constraints were examined in this section and used in the model.

To calculate the melt pool area, a procedure like that applied in single-track laser depositions was used to analyze in-situ thermal measurements with image processing in developed MATLAB® code and to obtain an appropriate comparison of melt pool size with process simulations for multi-layer deposited samples. Figure 5-21 shows an example image of

isometric view for 1500 W–12.5 mm/s case at the end of the last (8^{th}) layer build with temperature distribution. Figure 5-22, 5-23 and 5-24 shows the melt pool images on 2^{nd}, 5^{th}, and 8^{th} layers of a multi-layer deposition cases for eight deposited layers of thermal simulation and in-situ thermal measurements for 1500 W laser power–12.5 mm/s, 1500 W laser power–22.2 mm/s and 2500 W – 12.5 mm/s, respectively. The area and geometry of the melt pool geometry varies according to the distance from the substrate.

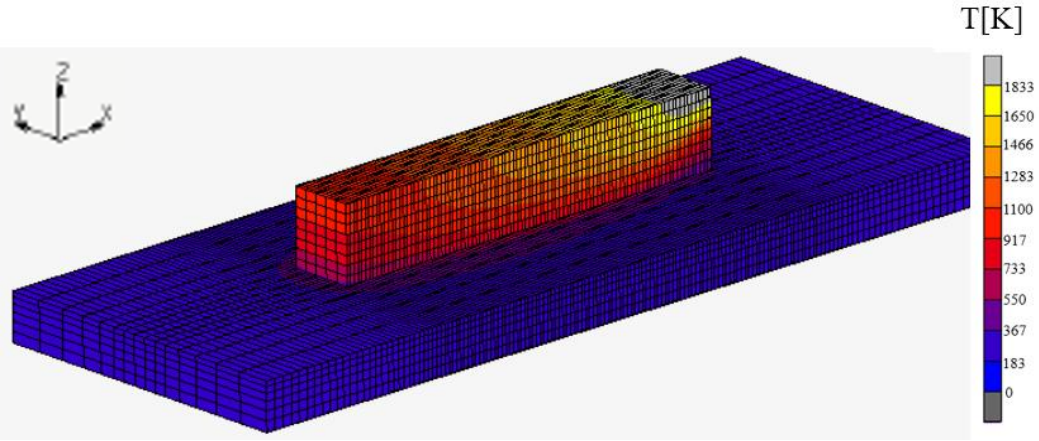

Figure 5-21 An example image to visualize isometric view of multi-layer model at the end of 8^{th} layer.

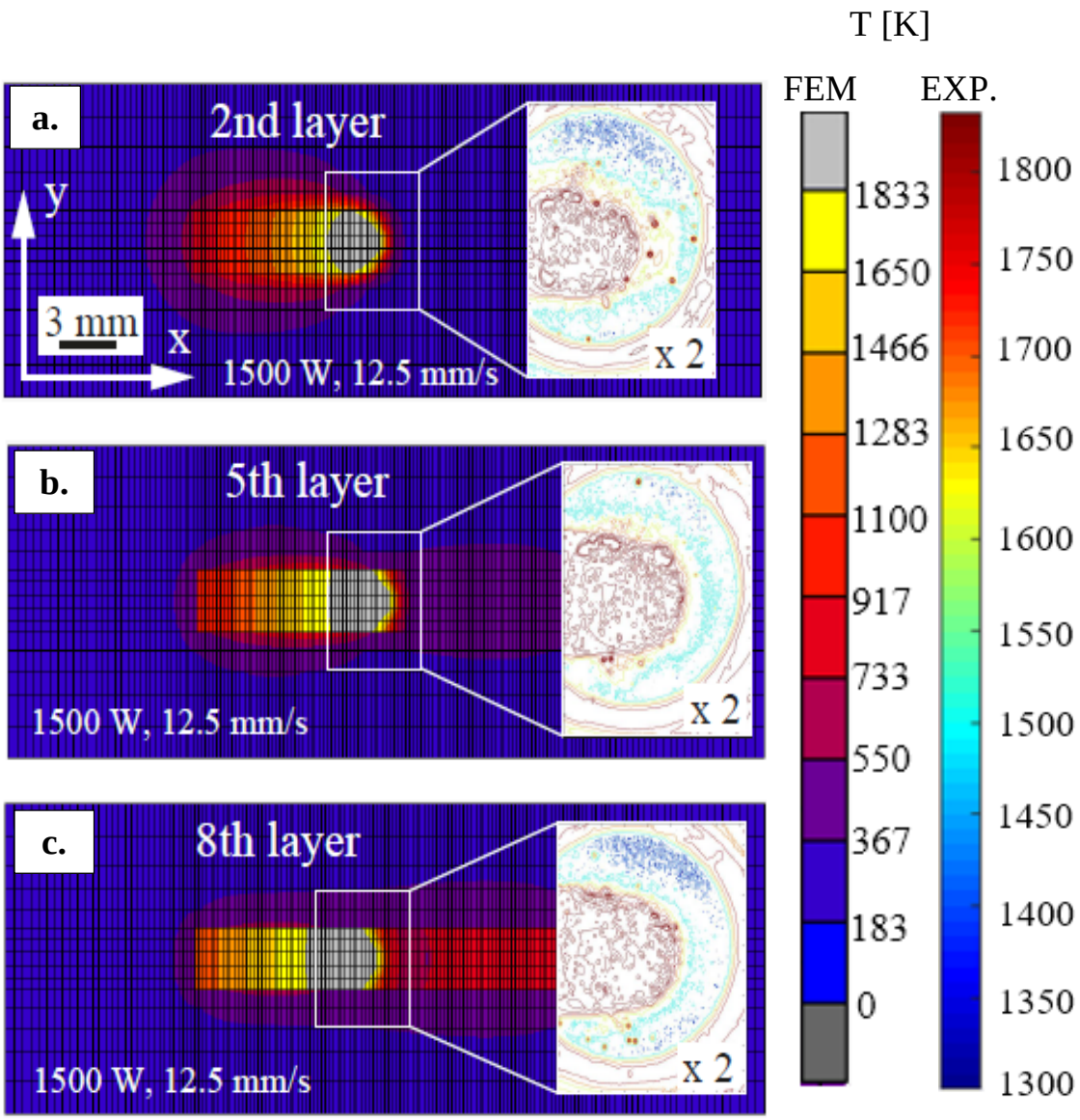

Figure 5-22 Temperature distributions of the simulations and in-situ melt-pool measurements for a multi-layer deposition. Top view of melt zone, a. 2nd layer, b. 5th layer, c. 8th layer for 1500 W - 12.5 mm/s.

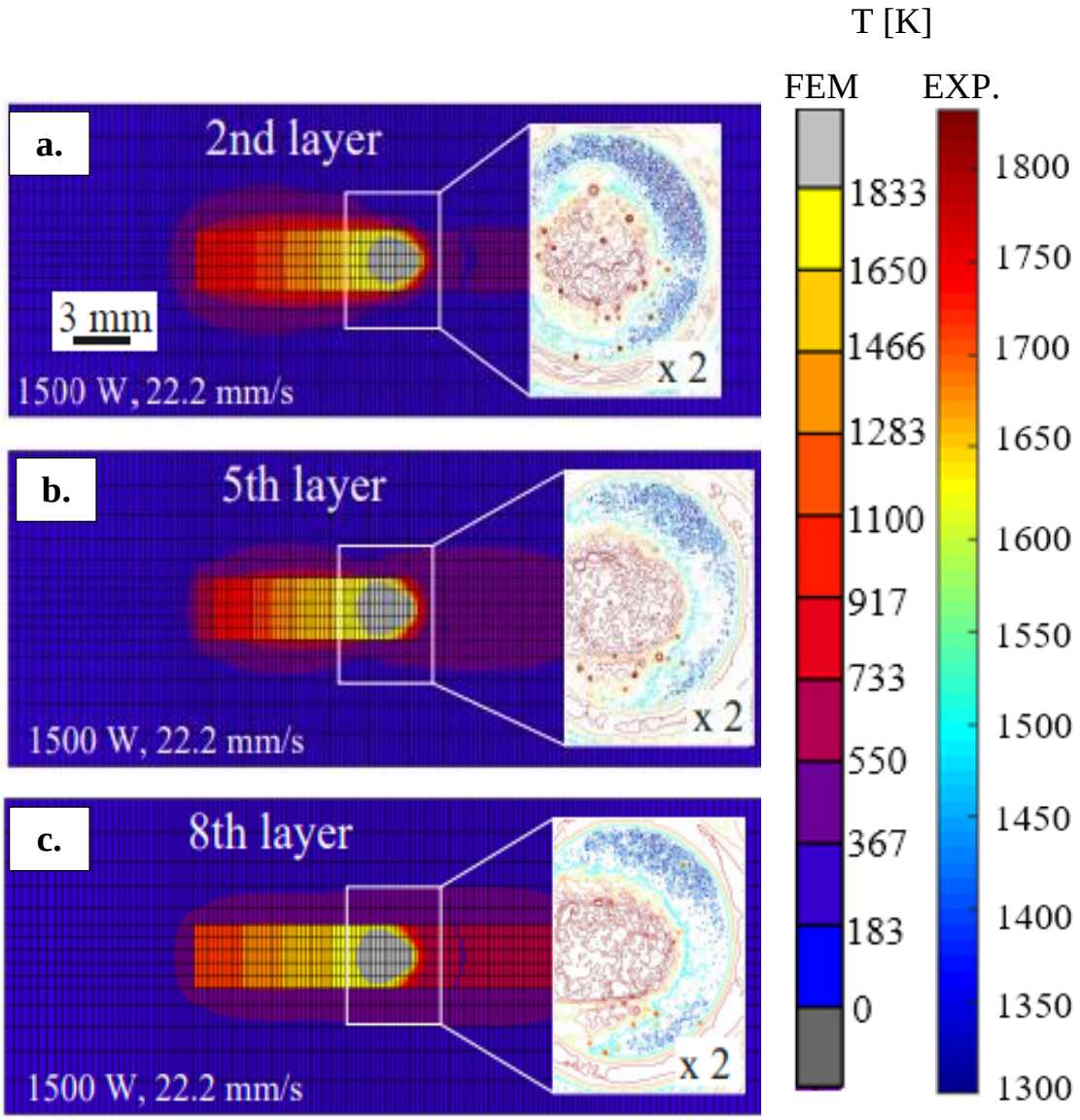

Figure 5-23 Temperature distributions of the simulations and in-situ melt-pool measurements for a multi-layer deposition. Top view of melt zone, a. 2nd layer, b. 5th layer, c. 8th layer for 1500 W - 22.2 mm/s.

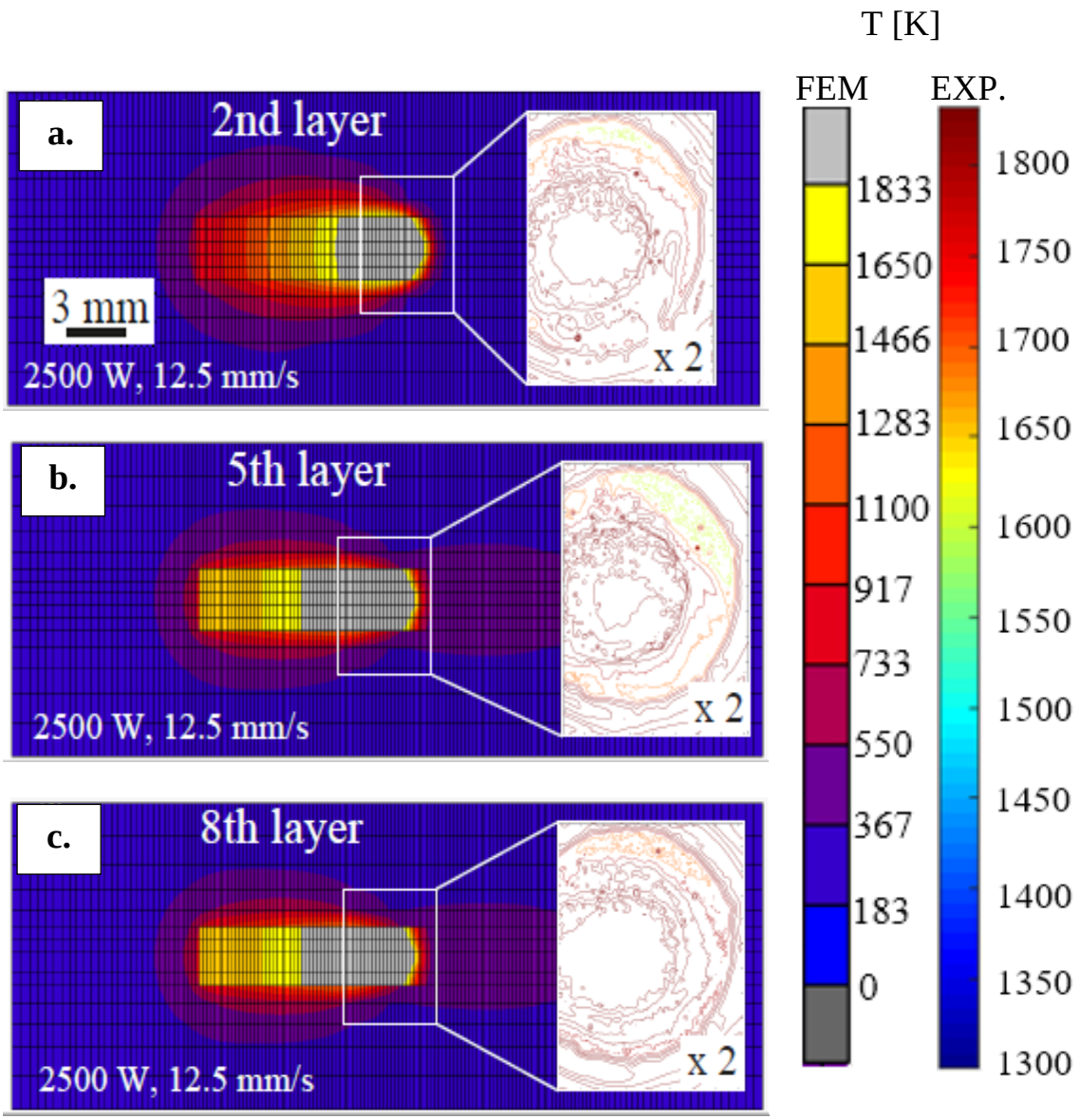

Figure 5-24 Temperature distributions of the simulations and in-situ melt-pool measurements for a multi-layer deposition. Top view of melt zone, a. 2nd layer, b. 5th layer, c. 8th layer for 2500 W - 12.5 mm/s.

Table 5-4 shows the comparison of results between FE model simulations and DED experiments for the cases of multi-layer depositions as shown in Figure 5-22, 5-23 and 5-24. Simulations underestimated the area of the melt pool for all cases. The maximum deviation of the developed model from the experiments is about 15%, and it can be reviewed that a positive relation is captured between simulations and experiments and that the model is correctly correlated with the experiments. Three different cases modeled in multi-layer structures show that the increase in laser power increases the area of the melt pool. Conversely, increasing the scanning speed and causing a less effect on the local area affected by the heat input causes shrinkage in the HAZ and results in a contraction of the melt pool

area. Regardless of the parameter set, as the number of layers increases, the area of the melt pool geometry increases as the distance from substrate increases.

Table 5-4 For multi-layer depositions, melt pool area comparisons for experimental measurements obtained from in-situ thermal imaging vs. thermal simulations.

			Melt Pool Area		
Laser Power [W]	**Scan Speed [mm/s]**	**Layer No.**	**Experiment [mm^2]**	**Simulation [mm^2]**	**Error [%]**
1500	12,5	2	6,43	6,22	-3,3
1500	12,5	5	7,28	7,2	-1,1
1500	12,5	8	8,7	7,76	-10,8
1500	22,5	2	5,52	4,92	-10,9
1500	22,5	5	5,81	5,73	-1,3
1500	22,5	8	6,33	6,28	-0,8
2500	12,5	2	12,87	11,02	-14,4
2500	12,5	5	14,4	13,05	-9,4
2500	12,5	8	15,85	15,54	-2

5.5 Multi-Layer Inter-Fusion Measurements

The analysis of micrographs of multilayer deposits is used to calculate the interlayer fusion distance between successive layers and the melt pool area that varies with the number of layers. Figure 5-25 shows the application of the method used to define or measure the interlayer fusion distance from the analysis of sections obtained with OM and simulation findings for experiment and analysis with 1500 W laser power and 12.5 mm / s scanning speed process parameters.

As shown in Figure 5-25, the boundary formed between the 6th and 7th layers is clearly visible to observe. Although this is not the case for the model, the deposition with the most obvious and interpretable boundaries has been chosen to be able to sample and investigate here by observing the conditions of the experiments. However, not all inter-layer fusion boundaries can be observed in experimental micrographs for all consecutive layers. Another

interesting finding apart from the observed structure is the melt pool, which has an increased curvature at baseplate level compared to deposition on successive layers with decreasing cusps. This observation is noteworthy in both experiments and simulations and also confirms each other. Experimental boundary areas are not perfectly aligned and symmetrical with respect to the center of the building layer, as in model simulations due to imperfections present during deposition. However, good agreement was found between simulation findings and experimental measurements.

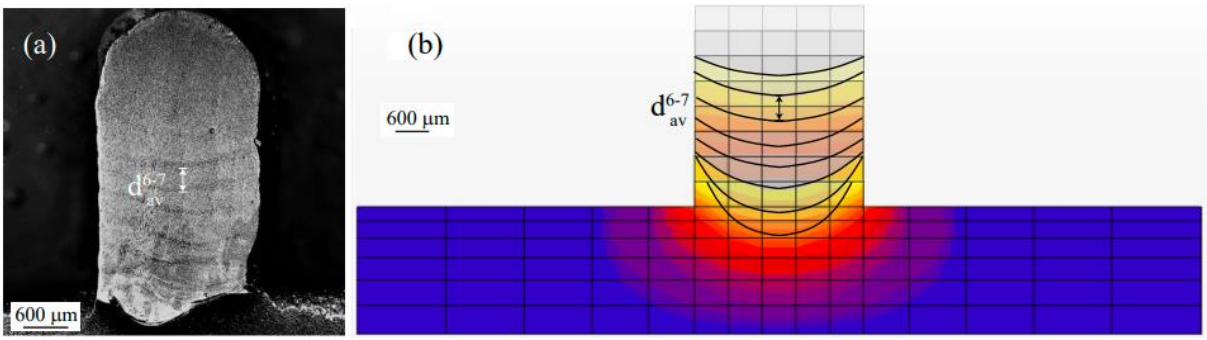

Figure 5-25 Average inter-layer fusion distance, example distance between 6th and 7th is indicated with the symbol d. a. Experimental from OM analysis, b. Melt zones obtained by superimposing the results of FE simulations for the case with 1500 W laser power and 12.5 mm/s scan speed.

6. CONCLUSION

For the DED process, a thermal process simulation model which includes the examination of both single-track and multi-layer depositions, with IN718 material is used as feedstock, has been developed and compared with the experimental study for the melt pool dimensions. The experiments carried out include processing the temperature data collected via in-situ monitoring during manufacturing of each sample under different process parameter conditions for both single-track and multi-layer depositions into temperature distribution contour maps by using the developed analysis code and examining the cross-sectional areas of the samples ex-situ by metallographic sample preparation. As a result of the studies carried out, the following conclusions have been reached.

- The thermal model developed uses a method of surface heat losses expressed in terms of a volumetric heat sink term to eliminate the need to redefine free surfaces using an additional user-defined subroutine after each layer is added. This method effectively includes convective, radiative, and evaporating surface heat losses and reflects them on the model results.

- To understand the effect of laser power and scanning speed on the melt area for single-track depositions, the maximum difference of the melt pool area between in-situ thermal measurements and model simulation findings reached 17% for nine different cases. The results that are generally showed consistency and useful to validate the model. For single-track depositions, the melt pool depth and width estimated by the model have a maximum deviation of 36% and 24%, respectively, except these values seem to have generally consistent estimates. The sections reveal that the deposited material fused to the baseplate significantly, in a manner that is not represented in the model. The key factor for the emergence of this difference between experiments and the model is that the element used in simulations is represented as a uniform layer in any case. In the developed model, due to finite element modeling limitations, addition of each single element with a uniform thickness conducted throughout the width (fixed as 3 mm - laser beam diameter) of the deposited layer for both single track and multi-layer simulations. On the other hand, in the experiment scenario, although via CAD geometry transferred to the machine over the digital based file is tried to be manufactured, the thickness of the layers does not process uniformly and vary in the

experimental practice. In addition, thermal loads that occur with the movement of the heat input in the feed direction and the resulting displacements are not considered in the thermal model, the deposited layer dilates and loses its geometric form. These findings are the main reasons for the error values that arise in the comparison between experimental work and model.

- The melt pool area dimensions and interlayer fusion boundaries of the multi-layer deposition between experiments and simulations were examined, and it was observed that there was a maximum variation of 15%, which reveals the predictive capacity of the thermal model.

7. BIBLIOGRAPHY

[1] W. E. Frazier, "Metal additive manufacturing: A review," *Journal of Materials Engineering and Performance*. 2014.

[2] G. N. Levy, R. Schindel, and J. P. Kruth, "Rapid manufacturing and rapid tooling with layer manufacturing (LM) technologies, state of the art and future perspectives," *CIRP Ann. - Manuf. Technol.*, vol. 52, no. 2, pp. 589–609, 2003.

[3] J. P. Kruth, M. C. Leu, and T. Nakagawa, "Progress in additive manufacturing and rapid prototyping," *CIRP Ann. - Manuf. Technol.*, vol. 47, no. 2, pp. 525–540, 1998.

[4] S. A. Khairallah, A. T. Anderson, A. Rubenchik, and W. E. King, "Acta Materialia Laser powder-bed fusion additive manufacturing : Physics of complex melt fl ow and formation mechanisms of pores , spatter , and denudation zones," *Acta Mater.*, vol. 108, pp. 36–45, 2016.

[5] I. Gibson, D. W. Rosen, and B. Stucker, "Introduction and Basic Principles," in *Additive Manufacturing Technologies: Rapid Prototyping to Direct Digital Manufacturing*, Boston, MA: Springer US, 2010, pp. 20–35.

[6] G. N. Levy, "The role and future of the Laser technology in the Additive Manufacturing environment," *Phys. Procedia*, vol. 5, no. PART 1, pp. 65–80, 2010.

[7] J. Lee and V. Prabhu, "Simulation modeling for optimal control of additive manufacturing processes," *Addit. Manuf.*, vol. 12, pp. 197–203, 2016.

[8] S. M. Thompson, L. Bian, N. Shamsaei, and A. Yadollahi, "An overview of Direct Laser Deposition for additive manufacturing; Part I: Transport phenomena, modeling and diagnostics," *Addit. Manuf.*, vol. 8, pp. 36–62, 2015.

[9] T. Evolution, "Simulation of Laser-assisted Directed Energy Deposition of Aluminum Powder : Prediction of," 2019.

[10] A. J. Pinkerton, "[INVITED] Lasers in additive manufacturing," *Opt. Laser Technol.*, vol. 78, no. 0, pp. 25–32, 2016.

[11] S. K. Everton, M. Hirsch, P. I. Stavroulakis, R. K. Leach, and A. T. Clare, "Review of in-situ process monitoring and in-situ metrology for metal additive manufacturing," *Mater. Des.*, vol. 95, pp. 431–445, 2016.

[12] M. Galati and L. Iuliano, "A literature review of powder-based electron beam melting focusing on numerical simulations," *Addit. Manuf.*, vol. 19, pp. 1–20, 2018.

[13] T. DebRoy *et al.*, "Additive manufacturing of metallic components – Process, structure and properties," *Prog. Mater. Sci.*, vol. 92, pp. 112–224, 2018.

[14] A. Dass and A. Moridi, "State of the art in directed energy deposition: From additive manufacturing to materials design," *Coatings*, vol. 9, no. 7. MDPI AG, 2019.

[15] M. Megahed, H.-W. Mindt, N. N'Dri, H. Duan, and O. Desmaison, *Metal additive-manufacturing process and residual stress modeling*, vol. 5, no. 1. Integrating Materials and Manufacturing Innovation, 2016.

[16] S. J. Wolff, S. Lin, E. J. Faierson, W. K. Liu, G. J. Wagner, and J. Cao, "A framework

to link localized cooling and properties of directed energy deposition (DED)-processed Ti-6Al-4V," *Acta Mater.*, vol. 132, pp. 106–117, 2017.

[17] A. Azarniya *et al.*, "Additive manufacturing of Ti–6Al–4V parts through laser metal deposition (LMD): Process, microstructure, and mechanical properties," *J. Alloys Compd.*, vol. 804, pp. 163–191, 2019.

[18] A. Gisario, M. Kazarian, F. Martina, and M. Mehrpouya, "Metal additive manufacturing in the commercial aviation industry : A review," *J. Manuf. Syst.*, vol. 53, no. August, pp. 124–149, 2019.

[19] T. Yamazaki, "Development of A Hybrid Multi-tasking Machine Tool: Integration of Additive Manufacturing Technology with CNC Machining," *Procedia CIRP*, vol. 42, no. Isem Xviii, pp. 81–86, 2016.

[20] J. M. Wilson, C. Piya, Y. C. Shin, F. Zhao, and K. Ramani, "Remanufacturing of turbine blades by laser direct deposition with its energy and environmental impact analysis," *J. Clean. Prod.*, vol. 80, pp. 170–178, 2014.

[21] "Norsk Titanium | Norsk Titanium to Deliver the World's First FAA-Approved, 3D-Printed, Structural Titanium Components to Boeing." [Online]. Available: https://www.norsktitanium.com/media/press/norsk-titanium-to-deliver-the-worlds-first-faa-approved-3d-printed-structural-titanium-components-to-boeing. [Accessed: 12-May-2021].

[22] R. Cottam and J. Wang, "Characterization of microstructure and residual stress in a 3D H13 tool steel component produced by additive manufacturing," 2014.

[23] P. Michaleris, "Modeling metal deposition in heat transfer analyses of additive manufacturing processes," *Finite Elem. Anal. Des.*, vol. 86, pp. 51–60, 2014.

[24] J. Ding, P. Colegrove, J. Mehnen, and S. Williams, "A computationally efficient finite element model of wire and arc additive manufacture," pp. 227–236, 2014.

[25] E. R. Denlinger and P. Michaleris, "Effect of stress relaxation on distortion in additive manufacturing process modeling," *Addit. Manuf.*, vol. 12, pp. 51–59, 2016.

[26] N. Shamsaei, A. Yadollahi, L. Bian, and S. M. Thompson, "An overview of Direct Laser Deposition for additive manufacturing; Part II: Mechanical behavior, process parameter optimization and control," *Addit. Manuf.*, vol. 8, pp. 12–35, 2015.

[27] P. Foteinopoulos, A. Papacharalampopoulos, and P. Stavropoulos, "On thermal modeling of Additive Manufacturing processes," *CIRP J. Manuf. Sci. Technol.*, vol. 20, pp. 66–83, Jan. 2018.

[28] R. Xie *et al.*, "In-situ observation and numerical simulation on the transient strain and distortion prediction during additive manufacturing," *J. Manuf. Process.*, vol. 38, no. February, pp. 494–501, 2019.

[29] N. W. Klingbeil, J. L. Beuth, R. K. Chin, and C. H. Amon, "Residual stress-induced warping in direct metal solid freeform fabrication," *Int. J. Mech. Sci.*, vol. 44, no. 1, pp. 57–77, 2002.

[30] G. Vastola, G. Zhang, Q. X. Pei, and Y. Zhang, "Controlling of residual stress in additive manufacturing of Ti6Al4V by finite element modeling," *Addit. Manuf.*, vol. 12, pp. 231–239, 2016.

[31] K. Ren, Y. Chew, J. Y. H. Fuh, Y. F. Zhang, and G. J. Bi, "Thermo-mechanical analyses for optimized path planning in laser aided additive manufacturing processes," vol. 162, pp. 80–93, 2019.

[32] T. Mukherjee, W. Zhang, and T. DebRoy, "An improved prediction of residual stresses and distortion in additive manufacturing," *Comput. Mater. Sci.*, vol. 126, pp. 360–372, 2017.

[33] F. Montevecchi, G. Venturini, N. Grossi, A. Scippa, and G. Campatelli, "Finite Element mesh coarsening for effective distortion prediction in Wire Arc Additive Manufacturing," *Addit. Manuf.*, vol. 18, pp. 145–155, 2017.

[34] T. R. Walker, C. J. Bennett, T. L. Lee, A. T. Clare, I. Facility, and H. Oxford, "A validated analytical-numerical modelling strategy to predict residual stresses in single-track laser deposited IN718," *Int. J. Mech. Sci.*, vol. 151, no. December 2018, pp. 609–621, 2019.

[35] X. Liang *et al.*, "A modified method for estimating inherent strains from detailed process simulation for fast residual distortion prediction of single-walled structures fabricated by directed energy deposition," *Addit. Manuf.*, vol. 23, no. July, pp. 471–486, 2018.

[36] M. E. Stender *et al.*, "A thermal-mechanical fi nite element work fl ow for directed energy deposition additive manufacturing process modeling," *Addit. Manuf.*, vol. 21, no. March, pp. 556–566, 2018.

[37] M. Chiumenti, X. Lin, M. Cervera, W. Lei, Y. Zheng, and W. Huang, "Numerical simulation and experimental calibration of additive manufacturing by blown powder technology. Part I: thermal analysis," *Rapid Prototyp. J.*, vol. 23, no. 2, pp. 448–463, 2017.

[38] Z. Yan *et al.*, "Review on thermal analysis in laser-based additive manufacturing," *Opt. Laser Technol.*, vol. 106, pp. 427–441, 2018.

[39] L. E. Lindgren, H. Å. Häggblad, J. M. J. McDill, and A. S. Oddy, "Automatic remeshing for three-dimensional finite element simulation of welding," *Comput. Methods Appl. Mech. Eng.*, vol. 147, no. 3–4, pp. 401–409, 1997.

[40] A. Anca, A. Cardona, J. Risso, and V. D. Fachinotti, "Finite element modeling of welding processes," *Appl. Math. Model.*, vol. 35, no. 2, pp. 688–707, 2011.

[41] L. E. Lindgren, A. Lundb, A. Lundbäck, and L. E. Lindgren, "Modelling of metal deposition," *Finite Elem. Anal. Des.*, vol. 47, no. 10, pp. 1169–1177, 2011.

[42] B. Babu, A. Lundbäck, and L. Lindgren, "Prediction of Stress & Distortion during Additive Manufacturing of Ti-6Al-4V PREDICTION OF STRESSES & DISTORTION DURING ADDITIVE MANUFACTURING OF TI-6AL-4V," no. June, pp. 2018–2022, 2019.

[43] L. Lindgren, "Numerical modelling of welding," vol. 195, pp. 6710–6736, 2006.

[44] V. Manvatkar and T. Debroy, "Spatial variation of melt pool geometry , peak temperature and solidification parameters during laser assisted additive manufacturing process," no. January 2016, 2015.

[45] R. Ye, J. E. Smugeresky, B. Zheng, Y. Zhou, and E. J. Lavernia, "Numerical modeling

of the thermal behavior during the LENS®process," *Mater. Sci. Eng. A*, vol. 428, no. 1–2, pp. 47–53, 2006.

[46] P. Peyre, P. Aubry, R. Fabbro, R. Neveu, and A. Longuet, "Analytical and numerical modelling of the direct metal deposition laser process," *J. Phys. D. Appl. Phys.*, vol. 41, no. 2, 2008.

[47] Y. Fu, S. Xie, X. Xu, G. Huang, L. Cheng, and Y. He, "Optimization of processing parameters for laser powder deposition using finite element method," *J. Wuhan Univ. Technol. Mater. Sci. Ed.*, vol. 25, no. 5, pp. 832–837, 2010.

[48] B. D. La Batut, O. Fergani, V. Brotan, and M. Bambach, "Analytical and Numerical Temperature Prediction in Direct Metal Deposition of Ti6Al4V," *J. Manuf. Mater. Process.*, vol. 1, no. 1, pp. 1–14, 2017.

[49] S. M. Kelly and S. L. Kampe, "Microstructural Evolution in Laser-Deposited Multilayer Ti-6Al-4V Builds : Part II . Thermal Modeling," vol. 35, no. June, pp. 1869–1879, 2004.

[50] J. Gockel, J. Fox, J. Beuth, and R. Hafley, "Integrated melt pool and microstructure control for Ti-6Al-4V thin wall additive manufacturing," *Mater. Sci. Technol. (United Kingdom)*, vol. 31, no. 8, pp. 912–916, 2015.

[51] M. F. Gouge, J. C. Heigel, P. Michaleris, and T. A. Palmer, "Modeling forced convection in the thermal simulation of laser cladding processes," *Int. J. Adv. Manuf. Technol.*, vol. 79, no. 1–4, pp. 307–320, 2015.

[52] Z. Gan, G. Yu, X. He, and S. Li, "Numerical simulation of thermal behavior and multicomponent mass transfer in direct laser deposition of Co-base alloy on steel," *Int. J. Heat Mass Transf.*, vol. 104, pp. 28–38, 2017.

[53] K. Ren, Y. Chew, Y. F. Zhang, G. J. Bi, and J. Y. H. Fuh, "Thermal analyses for optimal scanning pattern evaluation in laser aided additive manufacturing," *J. Mater. Process. Technol.*, vol. 271, no. March, pp. 178–188, 2019.

[54] H. Ju, P. Xu, C. Lin, and D. Sun, "Test and temperature field of finite element simulation about the effect of scanning speed on 304 stainless layer's properties by laser cladding," *Mater. Res. Innov.*, vol. 19, pp. 9–13, 2015.

[55] X. Lu *et al.*, "Residual stress and distortion of rectangular and S-shaped Ti-6Al-4V parts by Directed Energy Deposition: Modelling and experimental calibration," *Addit. Manuf.*, vol. 26, no. August 2018, pp. 166–179, 2019.

[56] M. E. Stender *et al.*, "A thermal-mechanical finite element workflow for directed energy deposition additive manufacturing process modeling," *Addit. Manuf.*, vol. 21, no. April, pp. 556–566, 2018.

[57] Q. Yang, P. Zhang, L. Cheng, Z. Min, M. Chyu, and A. C. To, "Finite element modeling and validation of thermomechanical behavior of Ti-6Al-4V in directed energy deposition additive manufacturing," *Addit. Manuf.*, vol. 12, pp. 169–177, 2016.

[58] J. Cao, M. A. Gharghouri, and P. Nash, "Finite-element analysis and experimental validation of thermal residual stress and distortion in electron beam additive manufactured Ti-6Al-4V build plates," *J. Mater. Process. Technol.*, vol. 237, pp. 409–419, 2016.

[59] E. R. Denlinger, "Thermo-mechanical model development and experimental validation for metallic parts in additive manufacturing," *ProQuest Diss. Theses*, p. 231, 2015.

[60] K. Zhang, X. Shang, and W. Liu, "Realtime measurement of temperature field during direct laser deposition shaping," *Adv. Mater. Res.*, vol. 143–144, pp. 521–526, 2011.

[61] A. Segerstark, J. Andersson, and L. E. Svensson, "Evaluation of a temperature measurement method developed for laser metal deposition," *Sci. Technol. Weld. Join.*, vol. 22, no. 1, pp. 1–6, 2017.

[62] S. Liu, P. Farahmand, and R. Kovacevic, "Optical monitoring of high power direct diode laser cladding," *Opt. Laser Technol.*, vol. 64, pp. 363–376, 2014.

[63] Z. Yan *et al.*, "Effect of thermal characteristics on distortion in laser cladding of AISI 316L," *J. Manuf. Process.*, vol. 44, no. May, pp. 309–318, 2019.

[64] B. Carcel, J. Sampedro, I. Perez, E. Fernandez, and J. A. Ramos, "<title>Improved laser metal deposition (LMD) of nickel base superalloys by pyrometry process control</title>," *XVIII Int. Symp. Gas Flow, Chem. Lasers, High-Power Lasers*, vol. 7751, no. Lmd, pp. 775123-775123–9, 2010.

[65] Z. Sun, W. Guo, and L. Li, "Numerical modelling of heat transfer, mass transport and microstructure formation in a high deposition rate laser directed energy deposition process," *Addit. Manuf.*, vol. 33, p. 101175, May 2020.

[66] A. Malmelöv, "Modeling of Additive Manufacturing with Reduced Computational Effort; Simulation of laser metal deposition with Inconel 625," p. 32, 2016.

[67] Y. S. Lee and W. Zhang, "Modeling of heat transfer, fluid flow and solidification microstructure of nickel-base superalloy fabricated by laser powder bed fusion," *Addit. Manuf.*, vol. 12, pp. 178–188, Oct. 2016.

[68] K. C. Mills, *Thermophysical Properties of Selected Commercial Alloys*. 2011.

[69] G. A. Greene, C. C. Finfrock, and T. F. Irvine, "Total hemispherical emissivity of oxidized Inconel 718 in the temperature range 300-1000°C," *Exp. Therm. Fluid Sci.*, vol. 22, no. 3–4, pp. 145–153, 2000.

[70] L. Parry, I. A. Ashcroft, and R. D. Wildman, "Understanding the effect of laser scan strategy on residual stress in selective laser melting through thermo-mechanical simulation," *Addit. Manuf.*, vol. 12, pp. 1–15, 2016.

[71] MSC-Software-Corporation, "Volume D: User Subroutines and Special Routines," vol. D, p. 338, 2016.

[72] B. Bax, R. Rajput, R. Kellet, and M. Reisacher, "Systematic evaluation of process parameter maps for laser cladding and directed energy deposition," *Addit. Manuf.*, vol. 21, no. April, pp. 487–494, 2018.

[73] S. J. Wol *et al.*, "Experimentally validated predictions of thermal history and microhardness in laser-deposited Inconel 718 on carbon steel," vol. 27, no. March, pp. 540–551, 2019.

[74] T. Petrat, C. Brunner-Schwer, B. Graf, and M. Rethmeier, "Microstructure of Inconel 718 parts with constant mass energy input manufactured with direct energy deposition," in *Procedia Manufacturing*, 2019, vol. 36, pp. 256–266.

[75] J. C. Liu and L. J. Li, "Effects of process variables on laser direct formation of thin wall," *Opt. Laser Technol.*, vol. 39, no. 2, pp. 231–236, Mar. 2007.

[76] M. H. Farshidianfar, A. Khajepour, and A. P. Gerlich, "Effect of real-time cooling rate on microstructure in Laser Additive Manufacturing," *J. Mater. Process. Technol.*, vol. 231, pp. 468–478, May 2016.

[77] E. Toyserkani, A. Khajepour, and S. Corbin, "Laser cladding," 2004.

[78] J. L. Bennett, S. J. Wolff, G. Hyatt, K. Ehmann, and J. Cao, "Thermal effect on clad dimension for laser deposited Inconel 718 ﬡ," *J. Manuf. Process.*, vol. 28, pp. 550–557, 2017.

[79] C. M. Lin, "Relationships between microstructures and properties of buffer layer with Inconel 52M clad on AISI 316L stainless steel by GTAW processing," *Surf. Coatings Technol.*, vol. 228, pp. 234–241, Aug. 2013.